

**PRELIMINARY DESIGN, BUILD AND FLIGHT TESTING OF A VTOL
TAILSITTER UNMANNED AERIAL VEHICLE WITH HYBRID
PROPULSION SYSTEM**

**M.Sc. Thesis by
Miraç K. AKSUGÜR**

Department : Aeronautics and Astronautics Engineering

Programme : Interdisciplinary Programme

NOVEMBER 2010

**PRELIMINARY DESIGN, BUILD AND FLIGHT TESTING OF A VTOL
TAILSITTER UNMANNED AERIAL VEHICLE WITH HYBRID
PROPULSION SYSTEM**

**M.Sc. Thesis by
Miraç K. AKSUGÜR
(511071149)**

**Date of submission : 24 November 2010
Date of defense examination: 12 November 2010**

**Supervisor (Chairman) : Assoc. Prof. Dr. Gökhan İNALHAN (ITU)
Members of the Examining Prof. Dr. Mehmet Ş. KAVSAOĞLU (ITU)
Committee : Assoc. Prof. Dr. M. Turan SÖYLEMEZ (ITU)**

NOVEMBER 2010

FOREWORD

First, I would like to thank my advisor, Prof. Gökhan İnalhan, for giving me opportunity to be a member of his distinguished research team, widening my vision, providing world-class research environment, supporting me materially and morally, and introducing me UAV research area. Working under his supervision in Controls and Avionics Laboratory was a marvelous experience to me.

I am very grateful to Serdar Ateş for his effort during inertia and modeling tests, and his deep friendship with lots of good memories while working together.

In addition, I really thank to my parents; Veli Aksugür and Nurcihan Aksugür for their patience and support during my study in ITU. More, I would also like to thank to my uncle and aunt; Erdal and Nurten Aksugür whom I accept as my second parents for their endless and invaluable support during my university education. Last, I want to thank Nihan Algül for her very precious support. I cannot describe her meaning to me by using any word in any language.

November 2010

Miraç K. Aksugür

Aerospace Engineer

TABLE OF CONTENTS

	<u>Page</u>
TABLE OF CONTENTS.....	vii
ABBREVIATIONS.....	ix
LIST OF TABLES.....	xi
LIST OF FIGURES.....	xiii
SUMMARY.....	xiii
ÖZET	xiii
1. INTRODUCTION.....	1
1.1 Purpose of the Thesis	4
1.2 Hypothesis	4
2. PROPULSION SYSTEM.....	5
2.1 Qualitative Comparison of Candidate COTS Propulsion Systems.....	5
2.1.1 Propeller Propulsion System	5
2.1.2 Ducted Fan Propulsion System.....	6
2.1.3 Combining the benefits; Hybrid Propulsion Approach.....	9
2.2 Qualitative Comparison of Candidate COTS Propulsion Systems; scaled specific thrust concept	10
3. DESIGN REQUIREMENTS AND CONCEPTUAL DESIGN	15
3.1 Design Concepts, Drivers and Constraints.....	15
3.2 Trade-Off Analysis.....	16
4. OPTIMIZATION.....	19
4.1 Inputs.....	20
4.1.1 Component Based Constant Weight Inputs	20
4.1.2 Design Inputs.....	21
4.2 Basic Calculations.....	21
4.2.1 Empty Weight Calculation	21
4.2.1.1 Fuselage Skin Weight Modeling	21
4.2.1.2 Wing Weight Modeling	23
4.2.1.3 Stabilizer Weight Modeling	25
4.2.1.4 Structural Weight Modeling.....	28
4.2.2 Battery Weight Modeling.....	28
4.2.2.1 Battery Weight Modeling of the Propeller Propulsion System.....	28
4.2.2.2 Battery Weight Modeling of the EDF Propulsion System.....	29
4.2.3 Drag Coefficient Modeling	30
4.2.3.1 Drag Force Modeling for Aerodynamic Surfaces	31
4.2.3.2 Drag Force Modeling for Fuselage.....	32
4.3 Optimization	33
4.3.1 Defining the Optimization Problem.....	33
4.3.2 Requirements, Variables and Constraints of the Optimization Problem ..	34

4.3.3 Mathematical Formulation of the Problem and Objective Function.....	36
4.3.4 Optimization Methodology	37
4.3.4.1 Design of Experiments (DOE)	39
4.3.4.2 Full Factorial	40
4.3.4.3 Multi Objective Genetic Algorithm II (MOGA-II)	43
4.3.4.4 Genetic Algorithm.....	44
4.3.4.5 Genetic Algorithm for Multi-Objective Optimization	47
5. OPTIMIZATION PROCESS.....	49
6. WIND TUNNEL TESTS	61
7. VORTEX-LATTICE ANALYSIS.....	63
8. LONGITUDINAL STATIC STABILITY ANALYSIS	67
8.1 Determination of Component Moments	68
8.2 Wing Contribution.....	68
8.2.1 Tail Contribution	69
8.2.2 Fuselage Contribution.....	70
8.3 Determination of Stick Fixed Neutral Point.....	72
9. PROTOTYPING.....	75
10.FLIGHT TESTS	83
11.CONCLUSION AND RECOMMENDATIONS	87
REFERENCES	89

ABBREVIATIONS

CAD	: Computer aided drawing
CAM	: Computer aided manufacturing
CNC	: Computer numerical control
COTS	: Commercial off the shelf
DC	: direct current
DOE	: Design of experiments
EDF	: Electric ducted fan
ESC	: Electronic Speed Controller
FF	: Form factor
FOM	: Figure of merit
MTOW	: Maximum take off weight
OAV	: Organic aerial vehicle
UAV	: Unmanned aerial vehicle
VLM	: Vortex lattice method
VPP	: Variable pitch propeller
VTOL	: Vertical take off and landing

LIST OF TABLES

	<u>Page</u>
Table 3.1: Design criteria for Tailsitter UAV	15
Table 3.2: Design constraints for Tailsitter UAV.....	15
Table 3.3: Design constraints for Tailsitter UAV.....	17
Table 4.1: Specifications and weights of the selected COTS Components	20
Table 4.2: Operational requirements for the optimization problem	35
Table 4.3: Primal values and side constraints for the optimization problem	35
Table 4.4: Design constraints for the optimization problem.....	36
Table 4.5: Full factorial levels of the optimization problem.....	41
Table 4.6: Table of distribution of correlation matrix on DOE table	43
Table 5.1: Design summary of the optimization problem.....	50
Table 5.2: Broken constraints at unfeasible design points.....	51
Table 5.3: Design points of dominant design Set.....	58
Table 5.4: Comparison of initial design and selected design (ID:2478).....	59

LIST OF FIGURES

	<u>Page</u>
Figure 1.1 : a: T-wing concept demonstrator from University of Sydney [1], b: micro tailsitter UAV prototype from University of Arizona [6].	2
Figure 2.1 : Thrust (C_t) and power (C_p) coefficients vs. advance ratio, for Graupner 20x12 carbon folding propeller. These coefficients were found analytically by Dr. Martin Hepperle and the source data can be reached by his website.	6
Figure 2.2 : Specific thrust (T/P) vs. airspeed, for Graupner 20x12 carbon folder propeller.	7
Figure 2.3 : Specific thrust (T/P) vs. airspeed graph of Schübeler DS51 EDF unit, based on wind tunnel measurements, graphed by using the manufacturer's own data.	8
Figure 2.4 : Comparison of change of specific thrust values with airspeed. Propeller is Graupner 20x12; EDF system is Schübeler DS51.	8
Figure 2.5 : Estimated specific thrust changing for RASA 28.5x12 propeller	10
Figure 2.6 : T/P vs. airspeed comparison of the selected propulsion systems.	10
Figure 2.7 : Scaled specific thrust comparison of the selected propeller and EDF.	11
Figure 2.8 : Scaled specific thrust calculation methodology for EDF propulsion system.	12
Figure 2.9 : Scaled specific thrust calculation methodology for Propeller propulsion system.	13
Figure 2.10 : Scaled specific thrust comparison of both EDF and propeller propulsion systems in hover and hight speed condition.	13
Figure 4.1 : General design methodology of ITU Tailsitter UAV.	19
Figure 4.2 : Representation of the Variables in Geometric Sense.	23
Figure 4.3 : Geometrical description of tail anhedral.	26
Figure 4.4 : Battey weight calculation steps for propeller propulsion system	30
Figure 4.5 : Battey weight calculation steps for EDF propulsion system.	31
Figure 4.6 : Flowchart for the optimization problem.	40
Figure 4.7 : Full factorial fot 3 levels of 3 variables (27 experiments).	41
Figure 4.8 : Bad and good distribution of correlation matrix on DOE table.	43
Figure 4.9 : Distribution of correlation matrix on DOE Table.	43
Figure 5.1 : Design summary chart of the optimization problem.	51
Figure 5.2 : All design points for the optimization problem.	52
Figure 5.3 : Chart of broken constraints at unfeasible design points.	54
Figure 5.4 : Feasible design Points for the optimization Problem	54
Figure 5.5 : Pareto chart for optimum design points.	55
Figure 5.6 : Frequency histogram for takeoff weight of pareto design points.	56
Figure 5.7 : Frequency histogram for wing loading of pareto design points.	56
Figure 5.8 : Frequency histogram for wingspan of pareto design points.	57
Figure 5.9 : Frequency histogram for horizontal tail arm of pareto design points.	57

Figure 5.10 :	Frequency histogram for fan battery weight of pareto design Points..	57
Figure 5.11 :	Frequency histogram for Payload weight of pareto design points	58
Figure 5.12 :	Frequency histogram for cruise time of pareto design points.	58
Figure 5.13 :	Selected design set from the pareto chart.	59
Figure 5.14 :	Selected design point as optimum design point.	61
Figure 6.1 :	EDF and testbench system.	63
Figure 6.2 :	Wind tunnel test setup for EDF propulsion system.....	64
Figure 6.3 :	Graphical representation of the obtained wind tunnel data.	64
Figure 7.1 :	Derivative calculations by TORNADO code.....	66
Figure 7.2 :	Aerodynamic derivative calculations by TORNADO code.....	66
Figure 7.3 :	Aerodynamic Force calculations by TORNADO code	67
Figure 7.4 :	Graphical output of the given sizing data.	67
Figure 8.1 :	Illustration of stable (a), neutrally stable (b) and unstable (c) states.....	69
Figure 8.2 :	Illustration of wing's contribution to the pitching moment	70
Figure 8.3 :	Illustration of tail's contribution to the pitching moment.....	72
Figure 8.4 :	Fuselage moment slope determination diagram.....	73
Figure 8.5 :	Fuselage moment slope determination diagram.....	73
Figure 8.6 :	Effects of center of gravity position on neutral point.....	74
Figure 8.7 :	Effects of center of gravity position on neutral point.....	75
Figure 9.1 :	Illustration of pultrusion method.....	77
Figure 9.2 :	Illustration of RTM method	78
Figure 9.3 :	3D CAD illustration of ITU Tailsitter aircraft.	79
Figure 9.4 :	Stabilizer mold milling is in progress.....	80
Figure 9.5 :	Machined wing and fuselage molds	80
Figure 9.6 :	Illustration of wet lay-up method	81
Figure 9.7 :	Molds to be polished.....	81
Figure 9.8 :	Cutting fibers for lay-up method.	82
Figure 9.9 :	Wing mold and composite wing shell.	82
Figure 9.10 :	Wing structure and molds.	83
Figure 9.11 :	Fuselage structure and mold.....	83
Figure 9.12 :	ITU Tailsitter UAV	84
Figure 10.1 :	Receiver and gyro wiring diagram	86
Figure 10.2 :	ITU Tailsitter is ready for the flight test.....	87
Figure 10.3 :	Beginning of the flight test.....	87
Figure 10.4 :	ITU Tailsitter is ready for the flight test.	88
Figure 10.5 :	ITU Tailsitter is taking off	88
Figure 10.6 :	Fuselage structure and mold.....	75
Figure 10.7 :	ITU Tailsitter UAV	76

PRELIMINARY DESIGN, BUILD AND FLIGHT TESTING OF A VTOL TAILSITTER UNMANNED AERIAL VEHICLE WITH HYBRID PROPULSION SYSTEM

SUMMARY

As a kind of Vertical take off and landing capable unmanned vehicles, tailsitter UAVs with their combined VTOL and fixed-wing aircraft with full flight-speed regime capability provides a distinct alternative to rotary-wing and ducted fan UAVs. ITU tailsitter concept is tailored towards city and urban operations with possible autonomous recharging capability to allow 24 hour on demand reconnaissance and surveillance for traffic and law-enforcement. The development of manned tailsitter aircraft had begun as early as 1950's. Such manned tailsitter aircraft were hard to control especially during landing phase, as the early tailsitter aircraft did not have any stability augmentation system to help the pilots during the critical landing phase. However, as unmanned systems developed, the distinct tailsitter concept is realized again by using recent autopilot technology. In ITU tailsitter, a folding propeller system is used for hovering, vertical take-off, vertical landing and low speed transition mode, whereas an electric ducted fan (EDF) system is used for level and high speed flight mode where the propeller folds onto the fuselage in order to reduce drag. Initial system performance analysis with candidate propulsion units indicate that up to 35m/s cruise speed and maximum 90 minutes of flight endurance can be achieved while carrying 1.2 kg payload – a distinct performance in comparison to the same class rotary-wing and OAV alternatives. This flight time includes 3 minutes of vertical take-off and landing phase. After being proven the new tailsitter concept with hybrid electric propulsion system with the help of prototyping and several flight tests, a new concept with several usage areas, such as reconnaissance and surveillance for traffic and law-enforcement, scientific research, defense industry, is going to born.

DİKEY İNİŞ KALKIŞ YAPABİLEN HİBRİT İTKİ SİSTEMLİ BİR İNSANSIZ HAVA ARACININ ÖN TASARIMI, ÜRETİMİ VE TEST UÇUŞU ÇALIŞMALARI

ÖZET

Son yıllarda, yüksek gelişim ivmesi gösteren mikro elektromekanik sensörler , motor ve pil teknolojileri, insansız hava araçlarının kullanım alanlarında ve geliştirilen araç sayısında artışa yol açmıştır. 2009 yılı itibariyle 1200’ü aşkın insansız hava aracı modeli kısmen ülkelerin envanterlerine girmiş; kısmen geliştirilme aşamasında halen yollarına devam etmektedirler. İnsansız hava araçları; geleneksel; kısa mesafede iniş-kalkış yapabilen ve dikey iniş kalkış yapabilen özelliğe sahip olarak olarak üç sınıfa ayrılabilir. Dikey iniş kalkış yapabilen (DİKY) sabit kanatlı insansız hava araçları (İHA), döner kanatlı ve fan gövdeli İHA'lara nazaran çeşitli üstünlükler göstermektedir. Sabit kanatlı DİKY uçak konsepti, 1950’lerde insanlı uçaklar üzerinde denenmiş, fakat pilotların üzerindeki iş yükü nedeniyle uçuş testleri birçok kazayla sonuçlanmıştır. Pilot kontrolündeki yetersizlikler sonucunda 1960’ların başında, dünya üzerindeki tüm insanlı sabit kanatlı DİKY projeleri durdurulmuştur. Fakat gelişen yazılım ve donanım teknolojileriyle, bu tip hava araçları, 1990’lı yıllardan itibaren insansız olarak, küçük ölçeklerde denenmeye başlanmıştır. Sabit kanatlı DİKY İHA’ların avantajları göz önünde tutularak, İTÜ bünyesinde elektrikli itki sistemi sayesinde sessiz olan ve otonom olarak şarj işlemini gerçekleştirerek 24 saat kesintisiz trafik – kanun kaçakçılığı gözlemi ve takibi yapabilecek kabiliyetlerde olan bir DİKY insansız hava aracı tasarımı başlatılmıştır. Dikey iniş ve kalkış operasyonu sırasında kullanılacak büyük çaplı pervane ve yatay uçuş sırasında kullanılacak fan sistemini içeren elektrikli hibrit itki sistemi sayesinde, İTÜ’de geliştirilen İHA’nın dünya üzerindeki diğer insansız uçaklara nazaran daha yüksek performanslı olduğu görülmüştür. Yaklaşık olarak 3 dakikalık dikey iniş kalkış aşamasından sonra 90 dakika kesintisiz uçuş yapabilen ve 1.2 kg faydalı yük taşıma kabiliyetine sahip, dünyada bir benzeri olmayan İTÜ-İHA’nın, üretim ve uçuş testlerinden sonra kendini kanıtlayacağı ve sivil/askeri birçok kullanım alanına sahip olacağı öngörülmektedir.

1. INTRODUCTION

Tailsitter UAVs combine vertical take off and landing (VTOL) operation and relatively high speed capabilities in single airframe and such concept provides manifest advantages over the other VTOL aircraft concepts including helicopters and organic air vehicles (OAVs). As a result of the increasing requisition on efficient and silent UAV concepts which require no regular "runway" for urban-civilian applications, the design of ITU-BYU tailsitter concept is adopted for tailoring towards city and urban operations with possible autonomous recharging capability to allow 24 hour on demand reconnaissance and surveillance for various usage areas from traffic/law-enforcement to border patrolling. The design and development of manned tailsitter concepts had begun in the beginning of 1950s and many experimental aircraft are build and tested during the period between 1950 and 1960s. The pilots of such manned aircraft were in charge of the aircraft's attitude control by only looking at the displays and sensing the behaviors of the aircraft in an upside position with unfamiliar control inputs comparing to the helicopter pilots. Moreover, such manned aircraft had control problems especially during landing and hover-to-cruise transition phase, because of having no stability augmentation system which helps test pilots to reduce their extremely-high-workload. Therefore, none of the experimental tailsitter concepts have proven the advantages over helicopters or fixed wing aircrafts. As a result of several accidents mainly due to the high workload over the test pilots, the development of the manned tailsitter projects were backed off after mid 1960s. However, with the help of the advances in both hardware and software based technologies [1], [2], [3], the distinct tailsitter concept was realized and took place among the other VTOL UAVs. Likewise, there are many VTOL concepts have developed or still under development. Now, OAVs are the most popular ones that can be classified under tailsitter concepts. Besides, Allied Aerospace's iStar series Organic Air vehicles (OAV) and Honeywell's electric powered mini class OAV are the foremost examples that have wide range of application area on the world. On the other hand, although the OAVs show efficient static-low speed flight due to the shroud and duct around the propeller blades, such

ducted fan UAV concepts still have some aerodynamic problems especially about efficient forward flight regime and hover to cruise transition phase. In addition, OAVs with their internal combustion engines also suffer from high levels of noise during operation. Therefore, the noise problem makes these types of tailsitter UAVs unsuitable for "silent intelligence" in urban operational areas. Other examples to the mini-mid size tailsitter concepts are T-Wing and Heliwing. T-Wing was developed at the University of Sydney at 2000s [4], and Heliwing was developed by Boeing. However, both of these similar concepts are not size wise suitable for urban applications because of their noisy internal combustion engines. Besides, there are also several micro class tailsitter UAV concepts such as Brigham Young University's tailsitter UAV [5] and University of Arizona's coaxial propeller driven UAV [6]. Nevertheless, such micro size UAVs are not suitable for carrying "useful" payload and for servicing in severe weather conditions. Two of the discussed tailsitter concepts are seen in Figure 1 Since 2001, related to recently increasing technology on Lithium based batteries, aircraft designers have started to think out electric powered aircraft concepts [7].

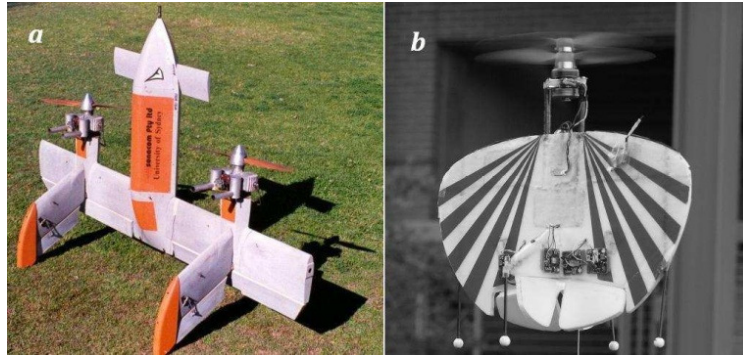


Figure 1.1 : a: T-wing concept demonstrator from University of Sydney [1], b: Micro tailsitter UAV Prototype from University of Arizona [6]

Moreover, advances in brushless DC electric motors have accelerated the development period of such kind of aircraft. In ITU Tailsitter, electric propulsion system choice as a major pre-design selection, because of electric powered propulsion's low noise levels and the unique capability to autonomously recharge the units from base landing stations. However, for an electric powered vehicle within the mini-UAV class, this unique capability calls for a trade-off between speed limited high power propeller configuration and the power limited high speed electric ducted fan (EDF) system. In this study, for mini class UAVs, design optimization and intuitive thrust-power-airspeed trade-off approach which leads to a hybrid "propeller-

ducted fan propulsion system” design that can achieve maximum horizontal flight time and maximum range for the ongoing ITU Tailsitter Project is provided.

Due to the aim of designing an efficient tailsitter UAV, propulsion system has the highest priority among the design requirements. Since electric powered propulsion system is also advantageous to internal combustion engines in terms of maintenance and noise level; electric propulsion system has been chosen as one of the requirements. Propeller driven system supplies high thrust to power ratio for VTOL operations. However, the thrust is rapidly decreased as the incoming airspeed is increased. Hence, the performance is decreased at high speed and the system becomes insufficient for cruise. On the other hand, Electric EDF system is capable of producing the same thrust with higher thrust to power gradient as the propeller system. Though the power consumption is increased, EDF system’s high thrust is necessary for long range cruise operations.

As a result, the hybrid propulsion system, consisting of both propulsion systems, was decided to be used in order to design an “all flight regime” efficient aircraft which meets the requirements. In ITU Tailsitter, a folding propeller system located on the nose of the aircraft, is used for hovering, vertical take-off, vertical landing and low-speed transition mode, whereas an EDF system, which is placed between the stabilizers, is used for level and high speed flight mode where the propeller folds onto the fuselage in order to reduce drag when it is turned off. In addition, to calculate the approximate empty weight calculation, instead of the classic method of empty weight fraction, “aircraft-based” weight modeling and optimization study have been conducted in order to see the most efficient design which is possible. Initial system performance analysis with candidate propulsion units represent that up to 40m/s cruise speed and maximum 90 minutes of flight endurance can be achieved while carrying 1.5 kg of payload in 10kg of flying system with 3 minutes of vertical take-off and landing operation duration. - a distinct performance in comparison to the same class rotary-wing and OAV alternatives. In the proceeding sections, a trade off analysis is given and hybrid-dual propulsion approach with a qualitative analysis of the selected propulsion systems is described. This is followed by the design overview and the design and design optimization approach. After that, the control methodology and the results are denoted.

1.1 Purpose of the Thesis

The three main objectives of this study are designing, prototyping and flight testing of an vertical take-off landing mini unmanned aerial vehicle with two different and discrete propulsion systems.

1.2 Hypothesis

This study provided a unique opportunity to use different propulsion systems for different flight conditions. Vertical takeoff landing air vehicles are generally designed to eliminate long runway for takeoff and landing phases of flight. Besides the VTOL capability, the vehicles are desired to ensure high speed cruise flight. However, for mini class unmanned aerial vehicles, it is hard to design a propulsion system allowing VTOL and cruise flight phases in one system. Therefore, in this thesis, using two different propulsion systems for two different flight regimes are discussed and being proven. According to the hypothesis, propeller propulsion system with relatively big diameter propeller is assigned to be work during vertical takeoff and landing missions; while the second electric ducted fan system with relatively small diameter, is desired to work under high speed cruise phase, because of its efficiency in high speeds.

2. PROPULSION SYSTEM

As well as the aerodynamic design, selection of the right propulsion system/component is utmost determinative on the performance of an aircraft. Comparing the propulsion systems of both “heavy lifter” helicopter and “fast and agile” jet fighter, it is comprehended that relatively high diameter and low weight loading propeller blades are efficient for hovering when relatively small diameter blades having high induced velocity, are used as effective way to reach high speeds. First, we compare the propeller and EDF propulsion systems separately with both qualitative and quantitative approach. Then we describe the advantages of combined propulsion system that we call “hybrid” propulsion.

2.2 Qualitative Comparison of Candidate COTS Propulsion Systems

2.2.1 Propeller Propulsion System

To select appropriate propeller for an aircraft, all the performance data of the candidate propellers should be carefully analyzed. Although there is a large number of available performance data about propellers [8], these propellers are mostly used on commercial or military manned aircraft. On the other hand, there is no sufficient and systematic cataloged propeller performance charts which are used on small scale UAVs, except for some test results [9].

In the analysis conducted, propeller performance is measured by plotting propeller coefficients against advance ratio (J) in Equation 2.1:

$$J = \frac{V_{\infty}}{n.D} \quad (2.1)$$

Here, V_{∞} denotes incoming air velocity, n is the revolution of propeller per second and D is the propeller diameter. For tailsitter UAV application, propeller system is considered to be used as primary lift generating device during VTOL operations. Thus, to get the highest specific thrust (T/P) value, a propeller having largest

diameter available and relatively low pitch value should be selected. Because, propellers having high pitch value are designed for high-speed applications and high percentage of propeller blades are stalled during zero speed (hovering) or low speed regimes (i.e. low speed vertical climb). To determine the specific propeller coefficients analytically, three important variables must be known; propeller chord distribution, airfoil twist distribution and airfoil data for each section of the blade. However, most of the commercially available hobby purpose propeller manufacturers do not provide such detailed information about their designs. For illustrative purposes, Graupner's carbon folding, 20x12 size (20 inches of diameter and 12 inches of pitch) propeller is considered. Figure 2.1 shows the thrust and the power coefficients against the advance ratio for this propeller; a commonly used propeller for this class of UAVs. After T/P ratio vs. airspeed conversion, the propeller data can be illustrated as given in Figure 2.2.

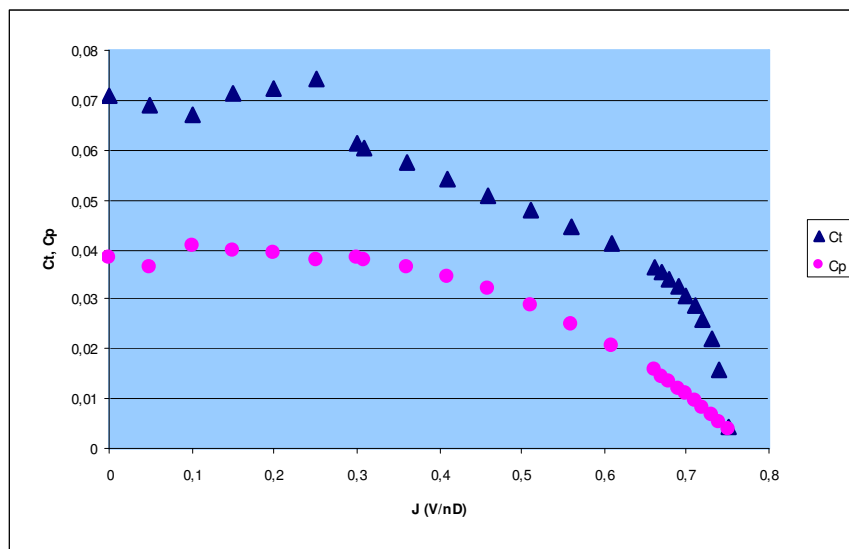


Figure 2.1 : Thrust (C_t) and power (C_p) coefficients vs. advance ratio, for Graupner 20x12 carbon folding propeller. These coefficients were found analytically by Dr. Martin Hepperle and the source data can be reached by his website [10].

2.2.2 Ducted Fan Propulsion System

There are many commercially available EDF units consisting of 3 to 7 blades regarding to their size and made from plastic or carbon fiber related to the working conditions. In addition, the commercially available EDF systems' diameters can vary between 5 and 14.5 cm.

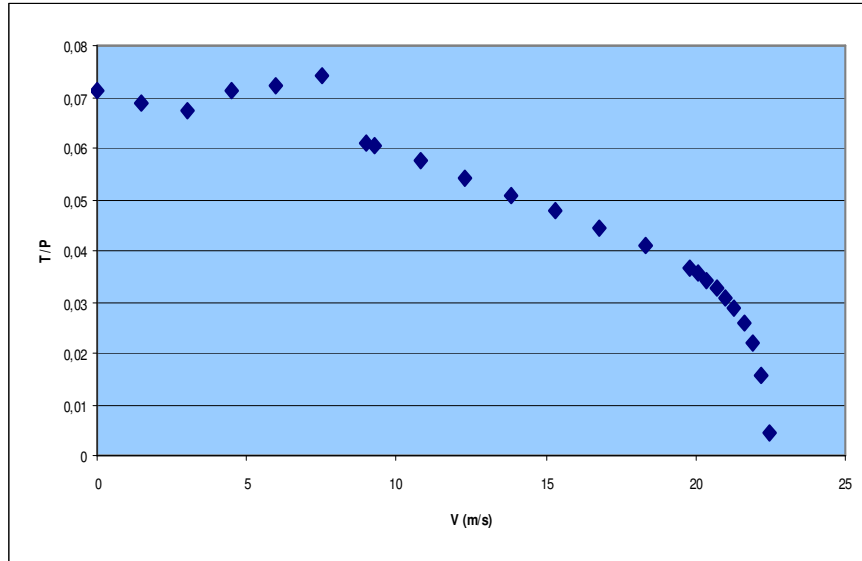


Figure 2.2 : Specific thrust (T/P) vs. airspeed, for Graupner 20x12 carbon folder propeller.

However, like small size propellers, hobby purpose EDF units also suffer from lack of any catalogued performance data. Moreover, they do not exhibit identical ducted fan behavior because of having wider gaps between shroud and blade tips than the full size precisely manufactured ducted fans. Many of the commercially available EDF systems are designed for high-speed applications, such as radio controlled model jets. In addition, at low speeds, for a given unit power input, EDFs produce less thrust than the propeller systems. Thus, EDF systems are suitable for relatively high cruise speed in comparison to the propellers. Hence, even though the T/P ratio of EDF systems are quite low at the static condition, second derivative of the T/P curve with respect to the airspeed is lower than the propellers' T/P curve's second derivative. Note that, there is only one unit with available wind tunnel test measurements, which is officially published on the manufacturer's website [8]. This is Schübeler brand's DS51 type EDF unit. According to the measurements, T/P vs. airspeed graphic for DS51 EDF system is shown in Figure 2.3.

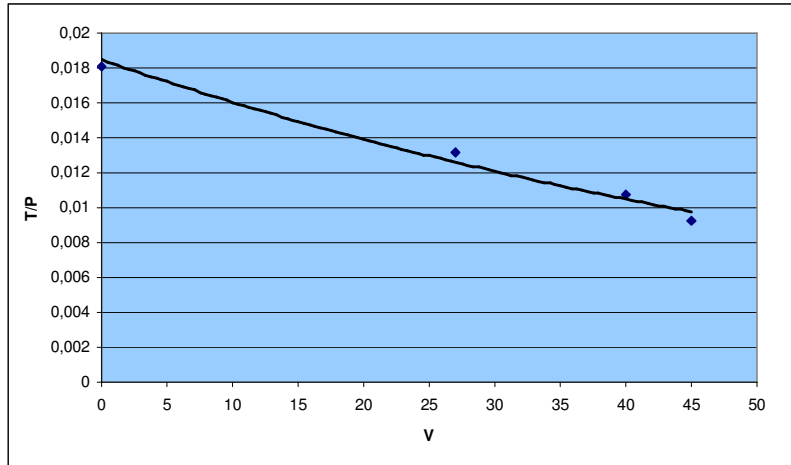


Figure 2.3 : Specific thrust (T/P) vs. airspeed graph of Schübeler DS51 EDF unit, based on wind tunnel measurements, graphed by using the manufacturer's own data

Because of the higher efflux velocity, specific thrust loss of EDF system in dynamic conditions is lower than the propeller system's loss, which in turn is advantageous for EDF systems in high-speed conditions. However, although the EDF unit can produce as much thrust as a propeller does, the power consumption at those thrust levels are much higher than the propeller system because of the lower T/P ratio. Therefore, EDF usage provides the ideal solution within the high speed flight while propeller system usage provides the ideal solution within the VTOL and low speed flight. This is illustrated in Figure 2.4.

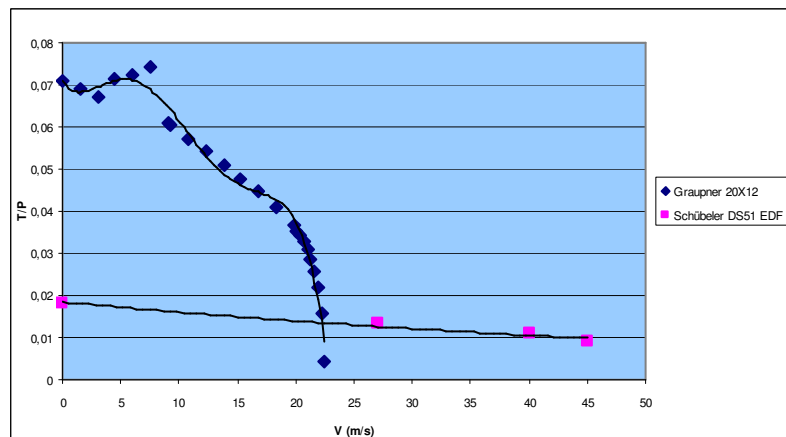


Figure 2.4 : Comparison of change of specific thrust values with airspeed. Propeller is Graupner 20x12; EDF system is Schübeler DS51.

For 20x12 propeller and Schübeler DS51 EDF combination, an active region of each propulsion system's usage is obvious. For VTOL (nearly static condition where V is zero) and transition up to 22.5 m/s velocity, propeller propulsion system can be considered to be active. After that, for cruising and high speed flying, propeller stops and fold onto fuselage and EDF system is activated to maintain desired airspeed above 22.5 m/s.

2.2.3 Combining the benefits; Hybrid Propulsion Approach

In this hybrid propulsion system, as discussed before, for both VTOL operations and hover to cruise transition phase, propeller system is used because of its energy efficiency. During cruising at high speed demand, EDF system is advantageous than propeller system. For the ITU tailsitter aircraft, the initial propeller selection is a RASA 28x12.5 size propeller and the EDF system is Schübeler DS51. Although there is wind tunnel test data for DS51 EDF system, the selected propeller unit has a measurement data only for static condition where incoming airflow is zero. Thus, some assumptions are made based on the performance values of the propeller propulsion systems to start the initial design process. The assumptions and the performance results for the selected propeller system take shape after inspecting the similar folding propellers' geometry. After making a comparison between RF brand 20x13, 20x12 and 23x12 propellers, it was seen that the chord distribution is almost directly proportional to size scaling. So, the chord length distribution for 28.5x12 RASA brand propeller is determined by using the similar chord distribution. After that, the twist distribution from the root of the propeller to the tip of the propeller is estimated in the light of the Graupner 20x12 and RASA 23x12 propellers' shape data. Because, the pitch values of both 20x12, 23x12 and 28.5x12 propellers are identical. Thus, both chord length and twist distribution of the selected propeller were entered to the propeller performance calculation software [11]. According to the results of the software, it is seen that the thrust and power coefficients nearly match with the static test results [12]. T/P curve based on the software can be seen in Figure 2.5.

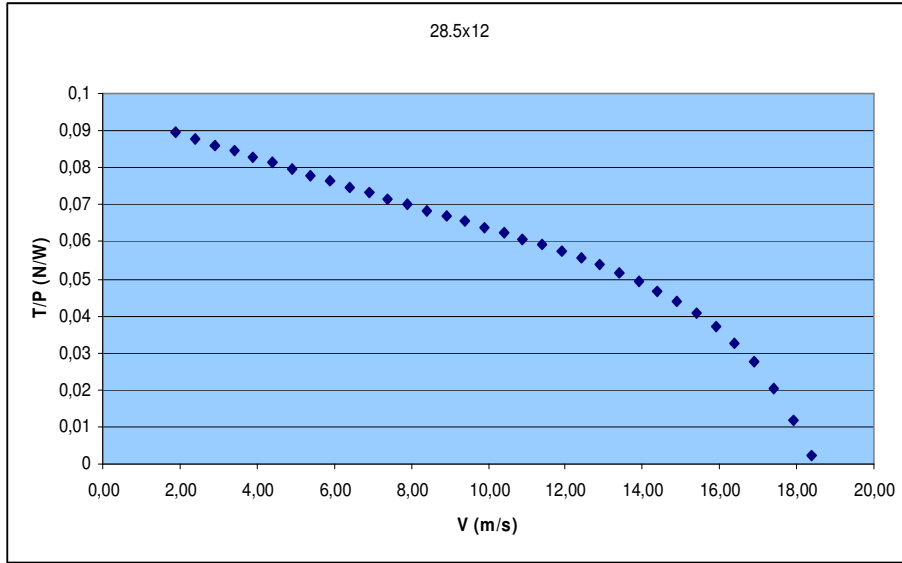


Figure 2.5 : Estimated specific thrust changing for RASA 28.5x12 propeller

As a result, the final T/P graphic for selected propulsion system can be seen in Figure 2.6. Note that, the initial condition is given for a constant thrust value. Hence, at zero speed, both of the systems are assigned the same thrust value.

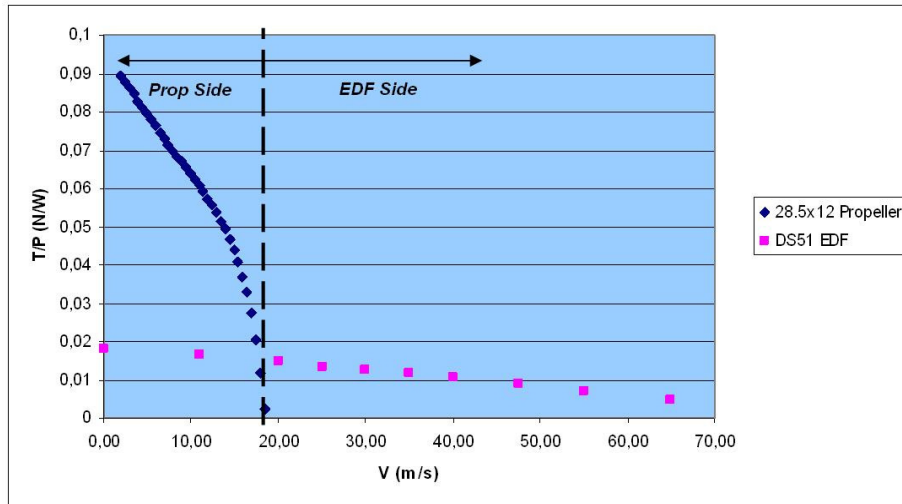


Figure 2.6 : T/P vs. airspeed comparison of the selected propulsion systems

2.3 Qualitative Comparison of Candidate COTS Propulsion Systems; scaled specific thrust concept

Specific thrust, which is defined as thrust to power ratio, is a preferential method to define and compare the efficiency values of propulsion systems. More,

since the specific thrust value is a function of advance ratio that is also a function of angular and airspeed, three dimensional complex surface geometry analysis should be conducted in order to see and quantize the performance of both of the propulsion systems. However, with the help of the scaled specific thrust method, which are structured during the design phase of ITU Tailsitter UAV, the three dimensional specific thrust determination problem has scaled down to two dimensional problem. To do that, x axis represents incoming air velocity, which is scaled from zero airspeed to the maximum desired airspeed, while y axis represents specific thrust values as seen in Figure 2.7. The calculation method of scaled specific thrust for both EDF and propeller propulsion systems is seen in Figures 2.8 and 2.9. Note that, for the selected “propeller based” propulsion systems, thrust and power coefficients can be written as a quadratic function of advance ratio. Therefore, the letters a_1 , a_2 , a_3 and a_2 , b_2 , c_2 in Figure 2.8 and Figure 2.9, are the coefficients of the quadratic equations of EDF and propeller systems respectively.

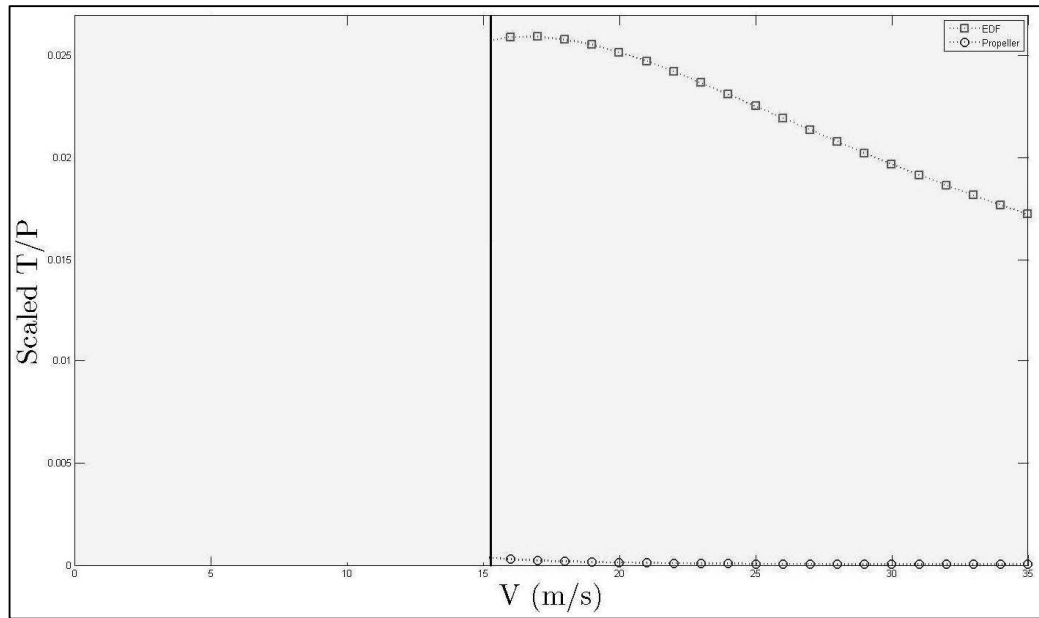


Figure 2.7 : Scaled specific thrust comparison of the selected propeller and EDF

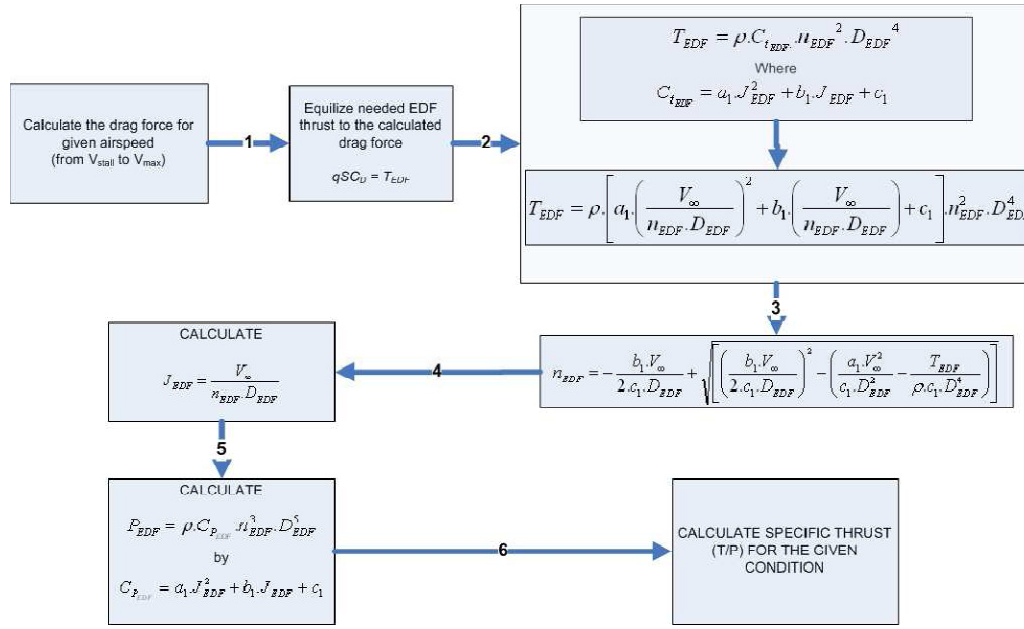


Figure 2.8 : Scaled specific thrust calculation methodology for EDF propulsion system.

In Figure 2.10, there are two regions, which are valid for our consideration. The first region is zero speed, which is simulated as hovering maneuver; the second region is from the black vertical line, which intersects the stall speed (16 m/s) on the x axis, to the desired maximum airspeed, which is 35 meters per second. The pink area between “very-low” speed (0-5m/s) and stall speed is intentionally left blank. This is because the simulation of exact and optimized transition maneuvers hasn’t been completed yet. To give more information, propulsion system only overcomes parasite and induced drag from the stall speed to the maximum airspeed. However, during the transition maneuvers, aircraft’s weight is added to drag component, which propulsion system must overcome. Therefore, the accurate transition phase airspeed is investigated after calculating the optimized transition maneuvers. As seen from Figure 2.10, each of the propulsion systems with any given airspeed condition results in different revolution per minute and advance ratio values. Therefore, the comparison between the propulsion systems can be made outright in Figure 2.10. Thus, the EDF system is about 64 times more efficient than the propeller system for the whole flight regime from stall to maximum airspeed.

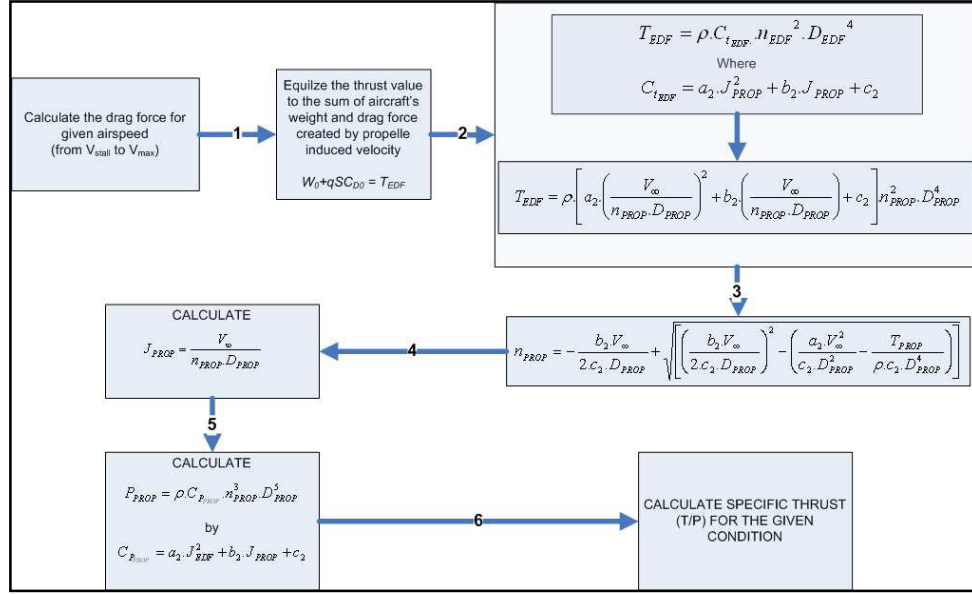


Figure 2.9 : Scaled specific thrust calculation methodology for EDF propulsion system.

Moreover, for static case analysis, specific thrust for both propeller and EDF systems are calculated as 0.1052 and 0.0122. Hence, depending on the static case calculations (for hover and low speed climb) it is seen that the propeller system is about 9 times more efficient than the EDF system. However, due to angular velocity restriction, the EDF system cannot produce adequate thrust as the propeller system.

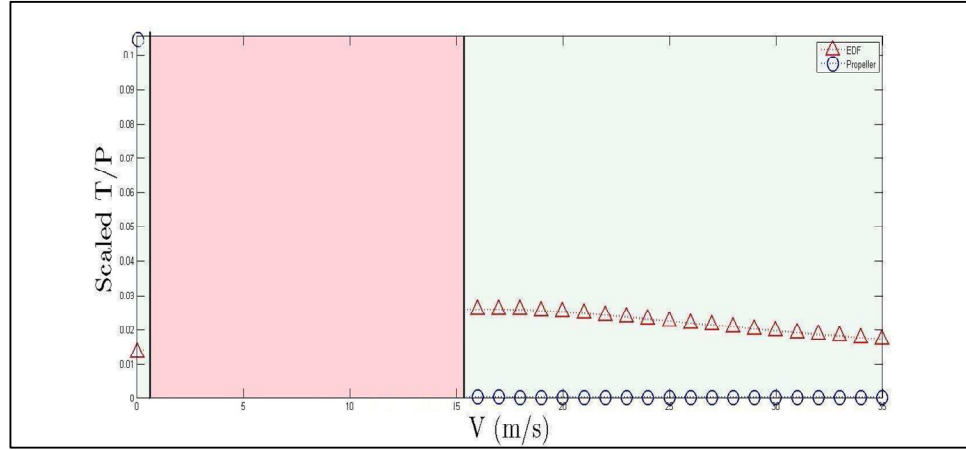


Figure 2.10 : Scaled specific thrust comparison of both EDF and propeller propulsion systems in hover and high speed condition.

As a result, the breakthrough advantage of the hybrid propulsion approach is seen as an evident in Figure 2.10.

3. DESIGN REQUIREMENTS AND CONCEPTUAL DESIGN

3.2 Design Concepts, Drivers and Constraints

The developed design philosophy hinges on obtaining the maximum possible payload capacity while achieving both high T/W ratio for VTOL and maneuverability and low energy demand per unit operation time (i.e. a low power demand for enhanced endurance).

Table 3.1 : Design criteria for Tailsitter UAV

Variables	Unit
Maximum Operation Condition Wind	15m/s
Minimum Range	20 km
Maximum Airspeed	35 m/s

To do this, an aircraft, which has a relatively high cruise speeds with vertical take off and landing capabilities, has been delineated. In addition, restrictions coming through

Table 3.2 : Design constraints for Tailsitter UAV

Specification	Limits
Operation Altitude	3000 ft
Portability	Backpackable
Minimum Operation Duration	30 minutes
Payload Volume	15x8x8 cm ³
Maximum VTOL Operation Area	1.4m x 1.4m

city operational environment were reflected via area and volume limitations before starting the design. The main design criteria and constraints can be seen in Table 3.1 and Table 3.2 respectively;

3.3 Trade-Off Analysis

For the most energy efficient flight, although a hybrid dual propulsion technique seems to be the ideal approach for this class of UAVs, a two-fold alternative trade-off can be considered in detail. First trade-off considered is the usage of a big EDF only propulsion system instead of the hybrid system. The reason for such a choice is that we can gain propeller propulsion system's weight to use as an extra battery weight by extracting the propeller propulsion system's weight. However, even if the EDF only configuration is advantageous over the hybrid propulsion system, there are two problems. First is the controllability problem. During hover conditions, the states of the aircraft are controlled by the aerodynamic force generator surfaces that are influenced by propulsion system's air-wash. Therefore, placing such force generator devices behind the EDF unit adds extra weight to the empty weight of the aircraft and reduces the efficiency of the EDF system both in hover and in cruise condition because of the additional drag. Thus, it is seen that the extra weight means less battery weight on the aircraft. Moreover, taking into consideration the controllability issues, placing the control vanes behind the relatively small diameter fan may not generate the adequate force to support the external disturbances and increases the cruise to hover transition time. In this manner, using the hybrid propulsion system increases the flight efficiency and aircraft's controllability during VTOL and transition operations.

Second is a tradeoff between larger ducted fan systems called Organic Aerial Vehicles (OAVs) and the hybrid propulsion combination. Ducted fan UAVs (OAVs) which have shrouded propellers are advantageous over the propeller only systems. Nevertheless, there are three main disadvantages of OAVs. First of all, for forward flight condition, OAVs require excessive thrust because of the need to overcome the weight of the aircraft contributes to the drag force of the airplane. As second, the complex variable pitch system adds more weight that can reduce the payload capacity. Third, because of increasing parasite drag of the duct; ducted system loses its efficiency as the airspeed increases [13]. As another chart

style comparison, figure of merit (FOM) chart is seen in Figure 2, which also includes OAV and ducted propeller-at-tail configurations.

Table 3.3 : Figure of merit (FOM) for different types of tailsitter concepts

FOM	Agility	Payload Capacity	Endurance	High Speed Performance	Cruise Efficiency	Development Time	Ease of Build	Complexity	TOTAL
One Propeller Driven	1	1	0	-1	0	1	1	1	4
Coaxial Propeller Driven	1	0	-1	-1	0	-1	-1	-1	-4
OAV	-1	0	-1	-1	0	0	-1	0	-4
Twin Propeller Driven	1	0	0	-1	0	1	1	0	2
Ducted Propeller at Tail	0	0	-1	-1	0	-1	-1	-1	-5
One Propeller Driven w/ VPP	1	-1	-1	1	1	-1	-1	-1	-2
Coaxial Propeller Driven w/ VPP	1	-1	-1	1	1	-1	-1	-1	-2
OAV w/ VPP	-1	-1	-1	0	0	-1	-1	-1	-6
Twin Propeller Driven w/ VPP	1	-1	-1	1	1	-1	-1	-1	-2
Ducted Propeller at Tail w/ VPP	0	-1	-1	0	1	-1	-1	-1	-4
Hybrid Propulsion Driven	1	0	1	1	1	0	1	1	6

Note that, the point rating is limited between “-1” and “1”, where “-1” is negatively affected the result, when 1 is positively effective on the total points. Moreover, the “VPP” stands for “Variable Pitch Propeller”. As seen from Figure 2, the concept with hybrid propulsion system is the foremost type of aircraft, which is followed by one propeller driven and twin propeller driven (T-Wing, Heliwing)

tailsitter concepts. Note that, OAV concept has the lowest rank among the other concepts being examined. Therefore, before starting the design process, the FOM chart has shown the advantages of the concept equipped with hybrid/dual propulsion system.

4. OPTIMIZATION

The developed design philosophy hinges on obtaining the maximum possible payload capacity while achieving both high thrust to weight ratio for VTOL, maneuverability and low energy demand per unit operation time (i.e. low power demand for enhanced endurance). To do this, an aircraft, which has a relatively high cruise speeds with vertical takeoff and landing capabilities, has been delineated. In addition, restrictions coming through city operational environment were reflected via area and volume limitations before starting the design. In this section, the optimization design methodology for the ITU Tailsitter UAV is summarized. As indicated in Figure 4.1, the design methodology approach consists of three main phases.

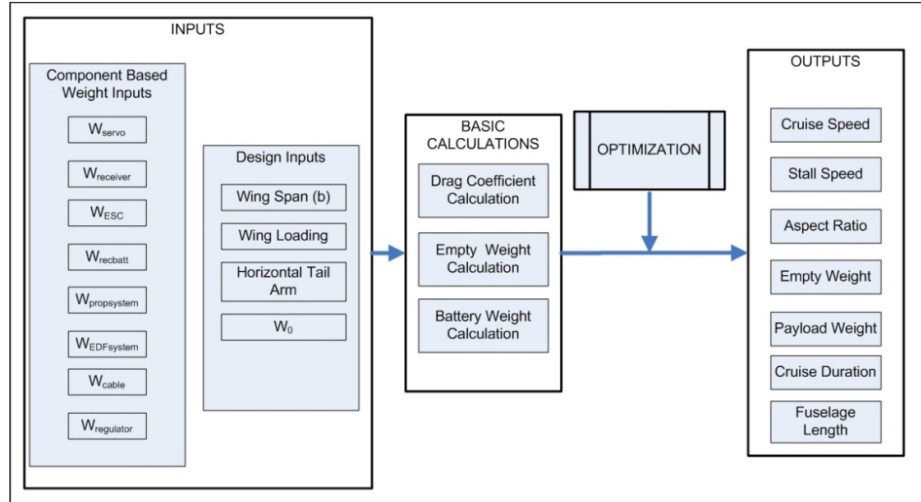


Figure 4.1 : General design methodology of ITU Tailsitter UAV

These phases are inputs, basic calculations and optimization. Input part includes two sub-parts. The first sub-part is called component based constant weight inputs, which includes the weights of the components that are fixed for the design process. The second sub-part is design inputs including wingspan, wing loading, maximum takeoff weight and the horizontal tail arm. In basic calculations part, drag coefficient, empty weight and battery weights are calculated. Optimization part is used to get most desirable design within our criteria and constraints.

4.2 Inputs

4.2.1 Component Based Constant Weight Inputs

In this part, non-variable weight inputs including electronic and power related equipments are summarized.

Table 4.1: Specifications and weights of the selected COTS components

Component	Specifications	# of Piece Used	Total Weight (gr)
Servo	JR-D58611 Digital Servo	103	215
Receiver	10 Channel, PCM Modulation	214	45
Receiver Battery	7.4V Lithium-Polymer	120	84
Motor Driver Unit	Phoenix HV85 Brushless ESC	121	230
Voltage Regulator	7.4 Volts to 6V Converter Circuit	210	20
Propeller Unit	Brushless motor and propeller	20	557
EDF Unit	Brushless motor and EDF unit	53	450
Cables	Various Size from 12 AWG to 24 AWG	11	50

The components contributing this category are servos, a radio receiver, a receiver battery, electronic brushless motor drivers, a voltage regulator, cables and the brushless motors of the propulsion systems. Note that, the sum of the weight of the component based weight inputs are kept constant for each design for whole

optimization process. All the components are commercial off-the-shelf (COTS) equipments and seen in Table 4.1.

4.2.2 Design Inputs

Design inputs consist of four variables; wingspan, wing loading, horizontal tail arm and aircraft's maximum takeoff weight. Upper and lower bounds of these variables will be described and shown in optimization subsection.

4.3 Basic Calculations

4.3.1 Empty Weight Calculation

During the design process of a manned aircraft, empty weight fraction value is generally obtained using the historical data of the same size class aircraft. Nevertheless, it is hard to find any sufficient data to construct empty weight prediction. Consequently, in ITU Tailsitter design, a quasi exact weight prediction method has been developed to calculate the "more accurate" empty weight value in terms of aircraft size and total weight. Empty weight of the aircraft is composed of four main weight components as seen in Equation 4.1 and these are described in detail in the following subchapters;

$$W_{empty} = W_{fuselage} + W_{wings} + W_{stabilizers} + W_{structural} \quad (4.1)$$

4.3.1.1 Fuselage Skin Weight Modeling

Before starting the calculations, composite fabrication method had been selected. As mentioned previously, during cruise flight, the folding propeller folds onto the fuselage to reduce the drag and then the EDF system is activated. Moreover, in "cruise to hover" transition phase, EDF system is shut down and the propeller system is reactivated in order to perform a power efficient landing. It is important to notice that, unfolding process of the propeller requires symmetrical fuselage shape to prevent the propeller from destructing the fuselage skin. Therefore, in the light of this prediction, a symmetrical airfoil, NACA 642-015, was selected to shape the fuselage geometry. After that, the relation between fuselage surface area and fuselage weight was derived. The measurements on the selected fuselage airfoil show that the surface

area is about 0.303 m², for 1 meter of fuselage length. Therefore, the function for the fuselage weight can be written as given in Equation 4.2 in terms of surface area and composite skin's surface weight density.

$$W_{fuselage} = 0.303 \cdot l_{fuselage} \cdot \rho_{skincomposite} \quad (4.2)$$

It should be noted that, $l_{fuselage}$ is the fuselage length in meters and $\rho_{skincomposite}$ is the composite skin's surface weight density in N/m². However, fuselage length in Equation 4.2 is not a sufficient parameter for the optimization problem since fuselage length depends on horizontal tail arm (l_{HT}) and root chord of the wing (C_{root}) which are variables of the optimization problem. Hence, fuselage length is expressed in terms of these variables as given in Equation 4.3

$$l_{fuselage} = l_{nose} + \frac{1}{4}C_{wingroot} + l_{HT} \quad (4.3)$$

The variable l_{nose} , which is determined as a constant value of 0.4 meters, represents the distance, which is assigned by considering folding propeller's clearance, between the leading edge of the wing root and nose of the fuselage. Therefore, the equation of fuselage weight is derived and seen in Equation 4.4. Moreover, to make a geometrical sense, The variables, l_{HT} and C_{root} , are explained in Figure 4.2 .

$$W_{fuselage} = 0.303 \cdot (0.342 + l_{HT} + \frac{C_{wingroot}}{4}) \cdot \rho_{composite} \quad (4.4)$$

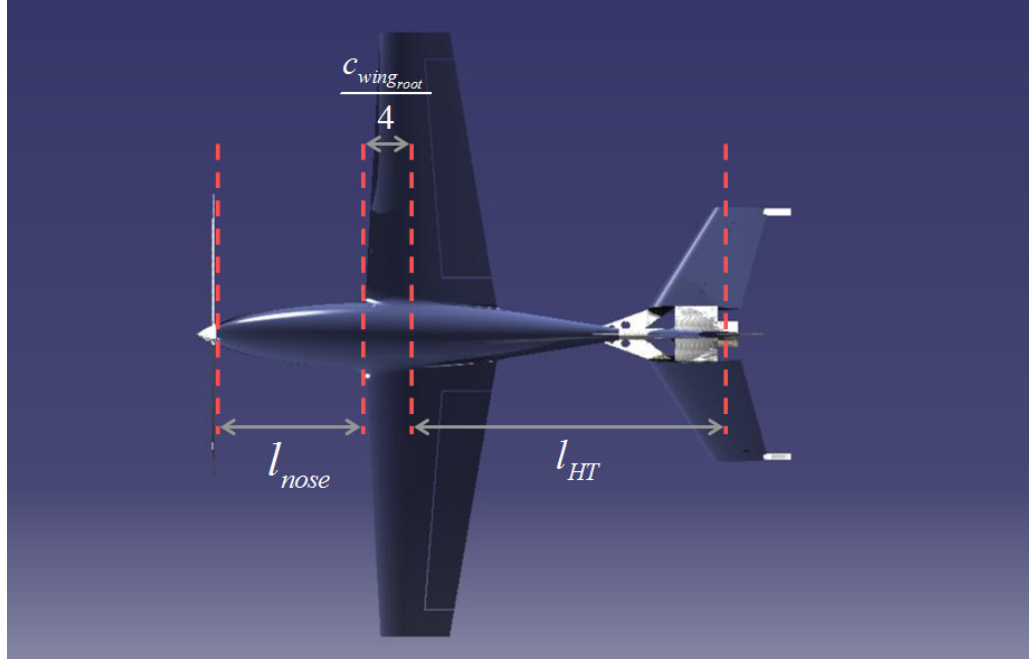


Figure 4.2 : Representation of the variables in geometric sense

4.3.1.2 Wing Weight Modeling

While obtaining wing weight function; wing airfoil, taper ratio, wing loading, wingspan are the main parameters. Hence, the calculations have been started with wetted surface area of the wing. Thus, for one meter of chord length, the wetted surface area is calculated as $2.06633b \text{ m}^2$, where b is wingspan. After that, the wing skin weight can be expressed as given in Equation 4.5:

$$W_{wingskin} = 2.06613 \cdot C_{mean_wing} \cdot b \cdot \rho_{composite} \quad (4.5)$$

It should be noted that, the production method and the material that is going to be used for both fuselage and wing are same. Moreover, the weight of wing spar, which is made of hollow carbon tube, must be obtained to derive the entire wing weight. Since the deflection at the tip of the wing is a crucial parameter for the wing stiffness, the tip deflection is restricted as 5 % of the wingspan upon having 2.5g of loading. According to the previous experiences, this loading condition can be modeled by applying the force, which is equal to half weight of the aircraft to the wing tip when the fuselage is stationary. As known from the mechanics of materials lectures, 2.5g load case for the half wing can be simulated as the tip deflection for cantilever beam that is loaded with concentrated force from the free edge. The

deflection is then expressed as given in Equation 4.6:

$$\delta = \frac{F \cdot l^3}{12 \cdot E \cdot I} = b \cdot 0.05 = \frac{\left(\frac{W_o}{2}\right) \cdot \left(\frac{b}{2}\right)^3}{12 \cdot E \cdot I} \quad (4.6)$$

For the equation given above, E is the modulus of elasticity of spar material and I represents moment of inertia for circular wing spar section. The moment of inertia can then be calculated in order to find the inner diameter of the spar, which is a hollow carbon tube. Note that, the outer diameter of the spar is restricted as given in Equation 4.7:

$$\phi_{\text{outerspar diameter}} = c_{\text{tip}} \cdot \left(\frac{t}{c}\right) - 0.003 \quad (4.7)$$

Where c_{tip} represents the wing tip chord, t/c represents thickness ratio of wing airfoil and the numerical value represents the thickness of skin composite material. After that, the moment of inertia can be calculated as given in Equation 4.8.

$$I = \frac{\pi}{4} \left[(\phi_{\text{outerspardiameter}})^4 - (\phi_{\text{innerspardiameter}})^4 \right] = \frac{\left(\frac{W_o}{2}\right) \cdot \left(\frac{b}{2}\right)^3}{12 \cdot E \cdot (b \cdot 0.05)} \quad (4.8)$$

More, the inner diameter of the spar can be expressed as seen in Equation 4.9.

$$\phi_{\text{innerspardiameter}} = \left[\frac{4 \cdot \left(\frac{W_o}{2}\right) \cdot \left(\frac{b}{2}\right)^3}{\pi \cdot 12 \cdot E \cdot (b \cdot 0.05)} - (\phi_{\text{outerspardiameter}})^4 \right]^{\frac{1}{4}} \quad (4.9)$$

Finally, the weight of the carbon spar can be calculated in Equation 4.10 and given as follows:

$$W_{\text{spar}} = \frac{\pi}{4} \cdot \left[(\phi_{\text{outerspardiameter}})^2 - (\phi_{\text{innerspardiameter}})^2 \right] \cdot b \cdot \rho_{\text{spar}} \quad (4.10)$$

For the equation given above, ρ_{spar} is the density of the carbon material per unit volume. Summing skin and spar weights, weight function for the wing is derived as given in Equation 4.11 given below.

$$W_{wing} = \frac{\pi}{4} \cdot \left[(\phi_{outerspardiometer})^2 - (\phi_{innerspardiometer})^2 \right] \cdot b \cdot \rho_{spar} + (2.06613 \cdot C_{mean_{wing}} \cdot b \cdot \rho_{composite}) \quad (4.11)$$

4.3.1.3 Stabilizer Weight Modeling

The total weight of the stabilizers can be expressed as the summation of horizontal and vertical tail weights. Manufacturing method applied for stabilizers is strictly different from the method applied for fuselage and wing. In this manufacturing technique, stabilizers are going to be made of high-density foam covered with carbon fiber. Therefore, wetted area and inner volume of the stabilizers are used to derive the weight function, given in Equation 4.12:

$$W_{HT} = S_{HT_{wetted}} \cdot \rho_{skincomposite} + v_{HT} \cdot \rho_{foam} \quad (4.12)$$

In Equation 4.11, $S_{HT_{wetted}}$ represents the wetted area of horizontal stabilizer in m^2 , $\rho_{skincomposite}$ represents the density of stabilizers' composite covering material in N/m^2 , v_{HT} represents the inner volume of horizontal stabilizer in m^3 , and ρ_{foam} represents the density of the foam that fills the horizontal tail in N/m^3 . As first step, horizontal stabilizer area can be written in terms of wing area, mean aerodynamic chord, tail arm and volume coefficient as seen in Equation 4.13, given below:

$$S_{HT} = \frac{V_{HT} \cdot \bar{c}_{wing} \cdot S_{wing}}{l_{HT}} \quad (4.13)$$

In the equation given above, V_{HT} is horizontal tail volume coefficient, \bar{c}_{wing} is wing mean aerodynamic chord of the wing, S_{wing} is wing area and l_{HT} is horizontal tail arm which is equal to the distance between quarter mean aerodynamic chords of wing and horizontal stabilizer respectively. In ITU Tailsitter airplane, inverted V-tail configuration is used with 25 degree of anhedral on both left and right horizontal stabilizer parts. Therefore, related to the anhedral angle, the actual area of horizontal stabilizer can be calculated by using Equation 4.14 and the figure representation is seen in Figure 4.3:

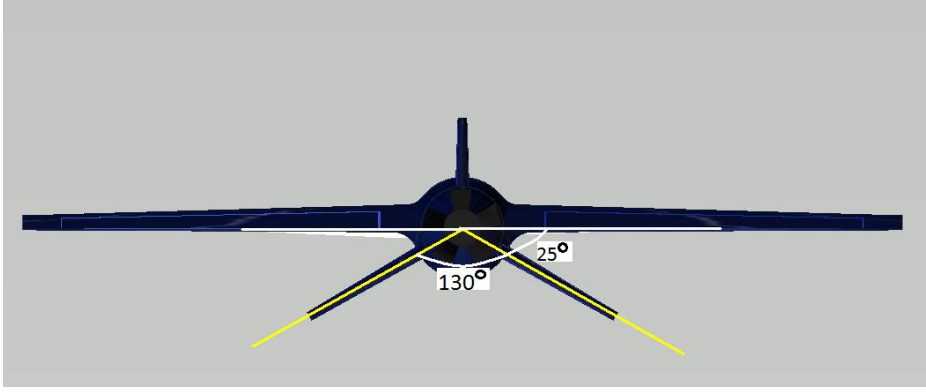


Figure 4.3 : Representation of the Variables in Geometric Sense

$$S_{HT_{actual}} = \frac{V_{HT} \cdot \bar{c}_{wing} \cdot S_{wing}}{l_{HT}} \cdot \frac{1}{\cos(25)} \quad (4.14)$$

After the actual horizontal tail area is determined, wetted area can be found with respect to the tail airfoil. As indicated before, NACA0014 is selected for horizontal and vertical stabilizers. Therefore, after inspecting the geometric properties of the selected airfoil, it is found that the wetted area is 2.133 m² per unit planform area, which can easily be found as given in Equation 4.15:

$$S_{HT_{wetted}} = 2.133 \cdot \frac{V_{HT} \cdot \bar{c}_{wing} \cdot S_{wing}}{l_{HT}} \cdot \frac{1}{\cos(25)} \quad (4.15)$$

After determination of wetted area for horizontal stabilizer, the weight of the composite skin covering material can be found as given in Equation 4.16:

$$W_{HT_{skin}} = 2.133 \cdot \frac{V_{HT} \cdot \bar{c}_{wing} \cdot S_{wing}}{l_{HT}} \cdot \frac{1}{\cos(25)} \cdot \rho_{skincomposite} \quad (4.16)$$

Next, the weight function for “foam core” must be found in order to derive weight function for horizontal tail. According to geometry, the airfoil side area coefficient for one meter of chord is determined as 0.000951. Hence, the volume of horizontal tail is expressed as given in Equation 4.17:

$$V_{HT} = \frac{V_{HT} \cdot S_{wing} \cdot C_{mean_{wing}}}{l_{HT}} \cdot \frac{1}{\cos(25)} \cdot (0.000951) \quad (4.17)$$

In order to determine the weight of foam core, the volume is multiplied by the foam density as given in Equation 4.18:

$$W_{foamcore} = \frac{V_{HT} \cdot S_{wing} \cdot C_{mean_{wing}}}{l_{HT}} \cdot \frac{1}{\cos(25)} \cdot (0.000951) \cdot \rho_{foam} \quad (4.18)$$

As a result, the total weight of the horizontal stabilizer is derived by summing both foam core and skin composite weights as seen in Equation 4.19:

$$W_{HT} = \left[2.133 \cdot \frac{V_{HT} \cdot C_{mean_{wing}} \cdot S_{wing}}{l_{HT}} \cdot \frac{1}{\cos(25)} \cdot \rho_{skincomposite} \right] + \left[\frac{V_{HT} \cdot S_{wing} \cdot C_{mean_{wing}}}{l_{HT}} \cdot \frac{1}{\cos(25)} \cdot (0.000951) \cdot \rho_{foam} \right] \quad (4.19)$$

Similarly, weight function for vertical tail can be derived by using the same steps and then obtained as Equation 4.20:

$$W_{VT} = \left[\left(\frac{V_{VT} \cdot S_{wing} \cdot b_{wing}}{l_{VT}} \right) - \frac{V_{HT} \cdot S_{wing} \cdot C_{mean_{wing}}}{l_{HT}} \cdot \tan(25) \cdot (2.113) \cdot \rho_{skincomposite} \right] + \left[\left(\frac{V_{VT} \cdot S_{wing} \cdot b_{wing}}{l_{VT}} \right) - \frac{V_{HT} \cdot S_{wing} \cdot C_{mean_{wing}}}{l_{HT}} \cdot \tan(25) \cdot (0.000951) \cdot \rho_{foam} \right] \quad (4.20)$$

Finally, entire weight function for stabilizers is derived by summing horizontal tail and vertical tail weight functions. By plugging Equation 4.19 and 4.20 in Equation 4.21, weight function for stabilizers is obtained as in Equation 4.22:

$$W_{stabilizer} = W_{HT} + W_{VT} \quad (4.21)$$

$$W_{stabilizer} = \left[\frac{V_{HT} \cdot S_{wing} \cdot C_{mean_{wing}}}{l_{HT}} \cdot \frac{1}{\cos(20)} \cdot (2.113) \cdot \rho_{skincomposite} \right] + \left[\frac{V_{HT} \cdot S_{wing} \cdot C_{mean_{wing}}}{l_{HT}} \cdot \frac{1}{\cos(20)} \cdot (0.000951) \cdot \rho_{foam} \right] + \left[\left(\frac{V_{VT} \cdot S_{wing} \cdot C_{mean_{wing}}}{l_{VT}} \right) - \frac{V_{HT} \cdot S_{wing} \cdot C_{mean_{wing}}}{l_{HT}} \cdot \tan(20) \cdot (2.113) \cdot \rho_{skincomposite} \right] + \left[\left(\frac{V_{VT} \cdot S_{wing} \cdot C_{mean_{wing}}}{l_{VT}} \right) - \frac{V_{HT} \cdot S_{wing} \cdot C_{mean_{wing}}}{l_{HT}} \cdot \tan(20) \cdot (0.000951) \cdot \rho_{foam} \right] \quad (4.22)$$

4.3.1.4 Structural Weight Modeling

Structural weight consists of the weight of spar box, bulkheads, longerons and glue. Spar box weight is assumed a constant, while glue weight can be approximated as 10 % of bulkheads, longerons and spar box weights. Moreover, for building fuselage frame, it is planned to locate four longerons along the fuselage and one bulkhead per each 0.15 meters of fuselage length. The total structural weight is then expressed as given in Equation 4.23:

$$W_{structural} = 1.1 \cdot \left[\frac{l_{fuselage}}{0.15} \cdot W_{bulkhead} + 4 \cdot l_{fuselage} \cdot W_{longeron} + W_{carrythrough} \right] \quad (4.23)$$

Where $W_{bulkhead}$ is the assigned constant average weight of a bulkhead, $W_{longeron}$ is the weight of a carbon longeron per unit length and $W_{carrythrough}$ is the assigned constant spar carrythrough weight. After determination of each component composing the equation, previously given as Equation 4.1, the empty weight can be written as summation of each component.

4.3.2 Battery Weight Modeling

4.3.2.1 Battery Weight Modeling of the Propeller Propulsion System

The propeller propulsion system is responsible for VTOL operations including hovering, low speed vertical climb and descent. To simplify the calculations, the total VTOL operation duration is set as 3 minutes with only hover mode. This is because, even though the propeller consumes more energy than hovering mode during vertical climb; the energy consumption level reduced below the level during hovering while vertical descent maneuver.

For hover mode, the thrust produced by the propeller is equal to the summation of weight of the aircraft and the drag force created by the propeller's induced velocity, which is calculated by using helicopter theory [14]. The battery weight determination logic for the propeller system is shown in Figure 4.4 systematically. The battery weight of the propeller propulsion system is a function of the VTOL operation duration, propeller's characteristics, airplane's geometry creating drag force and

the takeoff weight of the aircraft. Note that, in order to calculate the “worst case” and simplify the calculations, the parasite drag coefficient for whole aircraft is used, instead of the parasite drag coefficient that is constructed by the “induced velocity wetted” part of the aircraft.

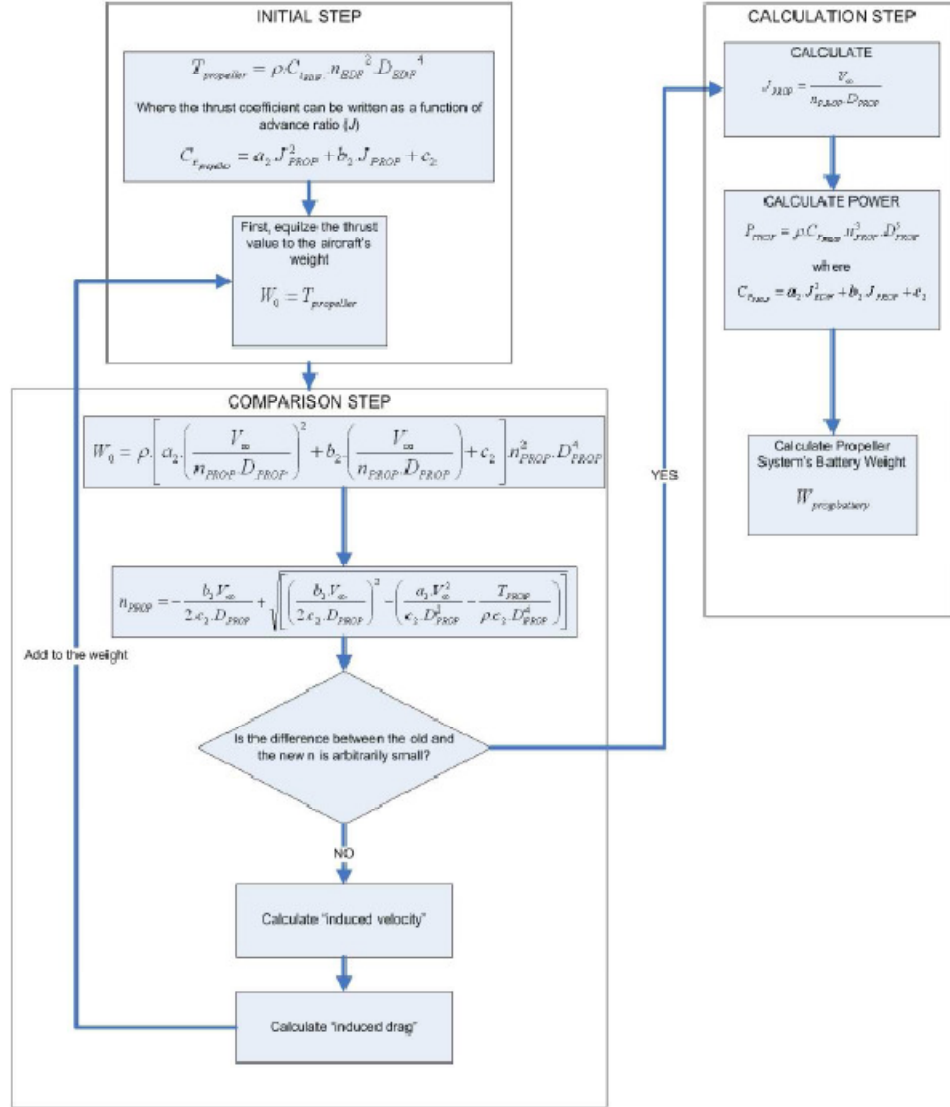


Figure 4.4 : Battery Weight Calculation Steps for Propeller Propulsion System

4.3.2.2 Battery Weight Modeling of the EDF Propulsion System

The selected EDF unit is mainly dedicated to cruise flight. For this reason, thrust generated by the EDF unit is equal to the drag force on the aircraft. Therefore, the battery weight calculation methodology is constructed on cruise flight and seen in Figure 4.5

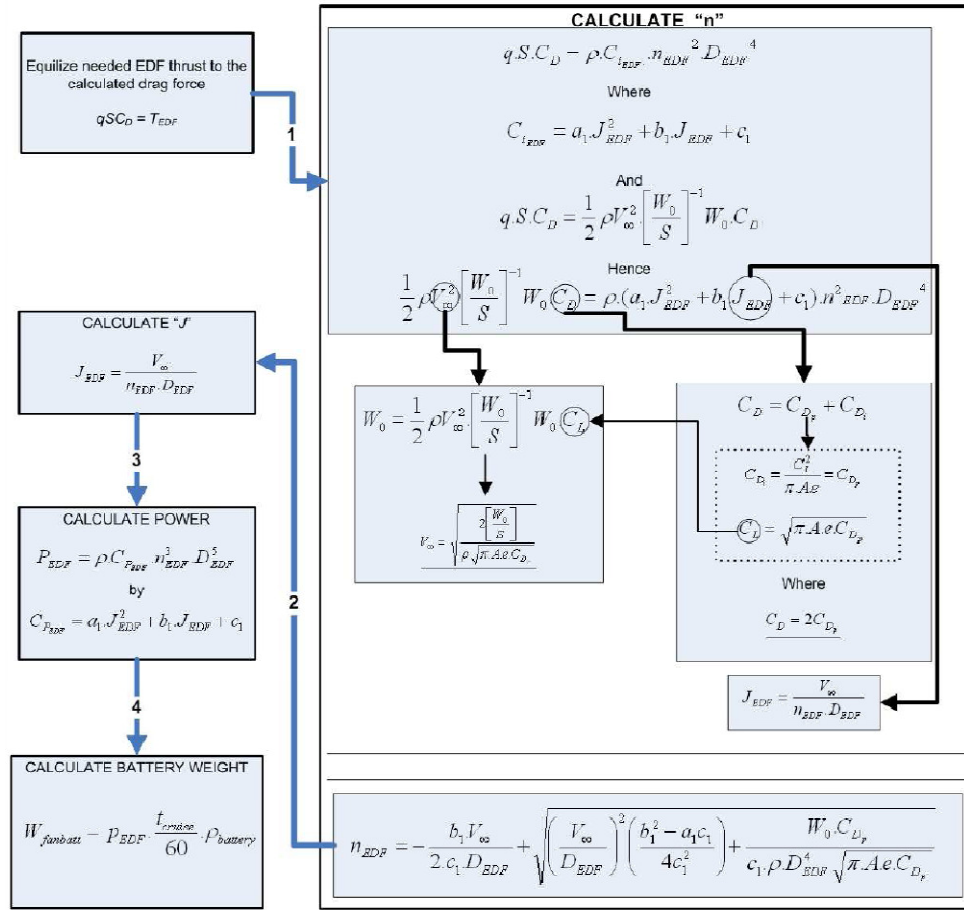


Figure 4.5 : Battery Weight Calculation Steps for EDF Propulsion System

4.3.3 Drag Coefficient Modeling

The drag force of an aircraft can be written as the summation of both parasite (zero lift) and induced drags. In ITU Tailsitter design, induced drag coefficient is equalized to the parasite drag coefficient so as to fly at “minimum thrust” level. According to drag coefficient assumption made, parasite drag coefficient is the only variable that must be formulated for each design during optimization process. To do that, the parasite drag coefficient of each of the components is calculated using the empirical “component buildup” method described by Raymer [15]. According to Raymer component buildup method is used to calculate drag

coefficient for sub-sonic flight and counts on both flat plate skin friction and component form factor (pressure drag due to the viscous separation). Related to component buildup method, the drag coefficient of each component can be described in Equation 4.24;

$$C_{D_p} = \frac{\sum C_{f_c} \cdot FF_c \cdot Q_c \cdot S_{wet_v}}{S_{ref}} + C_{D_{misc}} + C_{D_{LP}} \quad (4.24)$$

In Equation 24, C_f denotes flat-plate skin friction coefficient, FF represents form factors, Q indicates interference factor, S_{wet} is wetted area of the selected component and S_{ref} is the reference wing area. Where the subscript "c" indicates that those values are different for each component. In the following descriptions, the equations used for each component of the aircraft are shown.

4.3.3.1 Drag Force Modeling for Aerodynamic Surfaces

The parasite drag coefficient for the aerodynamic surfaces, C_{Daero} , composed of three discrete parts; wing, horizontal stabilizer and vertical stabilizer, and figured out in Equation 4.25:

$$C_{D_{aero}} = \frac{1}{S_{ref}} \left(C_{f_w} \cdot FF_w \cdot Q_w \cdot S_{wet_w} + C_{f_{HT}} \cdot FF_{HT} \cdot Q_{HT} \cdot S_{wet_{HT}} + C_{f_{VT}} \cdot FF_{VT} \cdot Q_{VT} \cdot S_{wet_{VT}} \right) \quad (4.25)$$

Flat-plate skin friction varies depending on the type of flow, laminar or turbulent, over the surfaces. For wing and stabilizers, turbulent flow assumption has been made and flat-plate skin friction coefficient is written as Equation 4.26

$$C_f = \frac{0.455}{(\log_{10} Re)^{2.58} + (1 + 0.144 \cdot M^2)^{0.65}} \quad (4.26)$$

Where "Re" represents Reynolds number, which is taken 500.000 for wings and 300.000 for stabilizers, "M" indicates mach number, which is selected 0.1 as constant for each design during optimization. To continue, form factor (FF) equation for wing and tails is written in Equation 4.27

$$FF = \left[1 + \frac{0.6 \cdot \left(\frac{t}{c} \right)}{\left(\frac{x}{c} \right)_{\max}} + 100 \cdot \left(\frac{t}{c} \right)^4 \right] \cdot \left[1.34 \cdot M^{0.18} \cdot (\cos \Lambda_m)^{0.28} \right] \quad (4.27)$$

In Equation 4.24, the term " $(x/c)_{\max}$ " is the chord wise location of the airfoil maximum thickness point, which is 0.3 for the selected airfoils of wing and stabilizers; Λ_m refers to the sweep of the maximum thickness line, which are 0 and 23 degrees for wing and stabilizers used in ITU Tailsitter, respectively. The interference factor, "Q", is chosen as 1.1 for both wing and stabilizers.

4.3.3.2 Drag Force Modeling for Fuselage

To calculate the drag coefficient for fuselage, the steps must be followed are similar to the steps followed in wing and stabilizer calculations. However, there is a change on form factor estimation. The form factor for fuselage or smooth canopy can be calculated using Equation 4.28

$$FF = \left(1 + \frac{60}{f^3} + \frac{f}{400} \right) \quad (4.28)$$

Where;

$$f = \frac{l}{d} = \frac{l}{\sqrt{\left(\frac{4}{\pi} \right) \cdot A_{\max}}} \quad (4.29)$$

In Equation 4.29, l is the length and A_{\max} is the maximum frontal area of the fuselage.

4.4 Optimization

4.4.1 Defining the Optimization Problem

During the preliminary design, it has been observed that an aircraft, which carries much more payload and flies longer, would be more challenging for the design. Therefore, optimization process is focused on maximizing payload weight and cruise duration. Since it is not possible to optimize all the design parameters, the parameters with crucial effect are selected as primal variables of the optimization problem. Maximum Takeoff Weight (W_0), Wing Loading (W/S), Wing Span (b), Horizontal Tail Arm (l_{HT}) and Fan Battery Weight ($W_{fanbattery}$) are determined as primal variables. The boundary constraints of those variables are going to be discussed in the 'Formulation Section'. In addition, the other design constraints for the optimization problem are going to be discussed in the same section as follows. Consequently, the optimization problem can be classified as multiobjective, multidisciplinary, constrained and continuous. It is a multiobjective problem because the objective is having a maximum payload capacity with maximum cruise duration. It is a multidisciplinary optimization problem because it consists of aerodynamics, propulsion, structure and design. It is a constrained optimization since it includes both boundary and design constraints which are going to be discussed later. It is a continuous problem since the variables are free to change within the side constraints. As it was stated before, the objectives of the optimization for the ITU Tailsitter UAV can be listed as follows;

- Maximization of payload weight
- Maximization of cruise duration

Assuming the Maximum Takeoff Weight (MTOW) as a constant; the objectives, given above, are in contradiction with each other. Since maximization demand on payload weight gives the minimum cruise duration while maximization of cruise duration, which also means maximization of the battery weight, minimizes the payload weight. In the light of such relations between the given objectives, the aim is to find the most suitable configuration by the optimization variables satisfying the design constraints.

4.4.2 Requirements, Variables and Constraints of the Optimization Problem

Before beginning the design process, design requirements were determined as seen in Table 4.2. After that, MTOW, wing loading, wingspan, horizontal tail arm and fan battery weight, which are listed in Table 4.3, are determined to be primal variables. The constraints of the primal variables are then considered as given in Table due to the listed reasons.

Table 4.2: Operational Requirements for the Optimization Problem

Variable	Values
Minimum Range	20 km
Minimum Operation Duration	30 minutes
Operation Altitude	1 km
Maximum Airspeed	50 m/s
Maximum Operation Condition Wind	15 m/s
Maximum VTOL Operation Area	2m x 2m
Minimum Payload Weight	0.8 kg

Table 4.3: Primal Variables and Side Constraints for the Optimization Problem

Primal Variable	Lower Bound	Upper Bound	Explanation
W_0	30N	100N	-
W_0/S	100 N/m ²	200 N/m ²	The limits are based on the similar type UAVs
b	1m	2m	-
l_{HT}	0.6m	1.5m	Structural limits during vertical landing phase.
$W_{fanbattery}$	3N	30N	The boundaries are set by the previous experiences

In addition to the side constraints, some operational and aerodynamic restrictions are also applied to the optimization problem to obtain the desired design. At the beginning, stall and cruise speeds are assumed crucial parameters for operation capability. Stall speed is limited up to 20 m/s where cruise speed is limited up to 50 m/s. Moreover, in order to prevent the aircraft stall due to the gust effects during cruise flight or landing approach, the cruise speed must be at least 5 m/s more than the stall speed. Second, although cruise duration and payload weight are being maximized as a result of the optimization algorithm, there are lower limits which come from the design requirements. In Table 4.2, it was stated that payload weight must be equal to or more than 0.8 kg, where the cruise duration must be at least 30 minutes. Next, in order to have an efficient, easily controllable and non-stubby design, the fuselage length is determined to be less than the wingspan. Moreover, aspect ratio's minimum value is set as 4. Consequently, all design constraints can be classified into three groups as operational capability, design requirements and geometrical limits. The determined design constraints of the optimization problem are then summarized in Table 4.4.

Table 4.4: Design Constraints for the Optimization Problem

Variables	Values
Operation Capability	$V_{stall} \leq 30 \text{ m/s}$
	$V_{cruise} \leq 50 \text{ m/s}$
	$V_{cruise} - V_{stall} \geq 5 \text{ m/s}$
Design Requirements	$t_{cruise} \geq 30 \text{ minutes}$
	$W_{payload} \geq 8 \text{ N}$
Geometrical Limits	$A \geq 4$
	$l_{fuselage} \leq b$

4.4.3 Mathematical Formulation of the Problem and Objective Function

In ITU Tailsitter design process, the main aim is to design an airplane which is configurable with different weight of payloads. To see the performance of the aircraft with different type (weight) of payloads, two objective functions have been defined; payload weight and cruise time. Therefore, in this multi-objective optimization problem, maximizing both of our objective functions is the main purpose.

Before explaining the objective functions, some descriptions should be made on the way that is following. Aircraft's maximum takeoff weight(W_0) can be expressed in Equation 4.30:

$$W_0 = W_{empty} + W_{payload} + W_{fanbattery} + W_{propbattery} + W_{inputs} \quad (4.30)$$

Where W_{inputs} is described in "Component Based ConstantWeight Inputs" section and can be rewritten in Equation 4.31.

$$W_{inputs} = W_{servo} + W_{rx} + W_{rxbatt} + W_{ESC} + W_{Vreg} + W_{cable} + W_{propunit} + W_{EDFunit} \quad (4.31)$$

In Equation 4.31; W_{servo} ; W_{rx} ; W_{rxbatt} ; W_{ESC} ; W_{reg} ; W_{cable} ; $W_{propunit}$; $W_{EDFunit}$ denotes the weights of servos, receiver, electronic speed controller of the brushless motors,

voltage regulator, cables, propeller propulsion unit and EDF unit respectively. In the light of the given formulations, one of the objective functions can be expressed in a compact form in Equation 4.32. Note that, W_{inputs} ; $W_{propbattery}$; $W_{fanbattery}$ and W_{empty} were described in the previous chapters as functions or invariant values.

$$W_{payload} = W_{payload} - \left(\begin{array}{l} W_{empty} + W_{fanbattery} \\ + W_{propbattery} + W_{inputs} \end{array} \right) \quad (4.32)$$

The second objective function is the cruise time for EDF propulsion system. As seen in Figure 4.5, the general process to determine the battery weight for the EDF system was summarized, but not formulated. Therefore, cruise time formulation, which is seen in Equation 4.33, is obtained with the help of the battery weight equation.

$$t_{cruise} = \frac{60 \cdot W_{fanbattery}}{\rho \cdot \rho_{battery} \cdot (a_2 \cdot J_{EDF}^2 + b_2 \cdot J_{EDF} + c_2) \cdot D_{EDF}^5} \cdot \frac{1}{\left[\frac{-b_1^2 \cdot v_\infty}{2 \cdot c_1 \cdot D_{EDF}} + \sqrt{\left(\frac{v_\infty}{D_{EDF}} \right)^2 \cdot \left(\frac{b_1^2 - a_1 \cdot c_1}{4 \cdot c_1^2} \right) + \frac{W_0 \cdot c_{Dp}}{c_1 \cdot \rho \cdot D_{EDF}^4 \cdot \sqrt{\pi \cdot A \cdot e \cdot c_{Dp}}}} \right]^3} \quad (4.33)$$

4.4.4 Optimization Methodology

After the optimization problem is discussed in detail, optimization process becomes ready to be carried through. Instead of developing a new code, the commercially available software is preferred for the multidisciplinary design optimization of ITU Tailsitter UAV and so Optimization process is decided to be performed by using Esteco ModeFRONTIER 3.2[16] and MicrosoftExcel commercial software, which are run simultaneously. Therefore, Esteco ModeFRONTIER software is selected as the main optimization driver tool and "Microsoft Excel" is selected for the analysis tool. In order to solve optimization problem, mathematical formulations, which are already given in the previous chapters, are written into the Microsoft Excel and a calculation Excel Sheet is obtained. After that, Esteco ModeFRONTIER is connected to Excel Sheet in order to perform the calculations. Next, the optimization flowchart is started to be built by adding five input nodes, which are also the previously considered optimization variables (W_0 , Wing Loading, Fan Battery Weight, Horizontal Tail Arm and Wing Span). The side constraints of optimization variables are then applied to these input nodes and seven output nodes are added to the

flowchart. Aspect Ratio, Cruise Speed, Stall Speed, Speed Difference and Fuselage Length output nodes are used in order to apply design constraints which are previously given in Table 4.3. More, Payload Weight and Cruise Time output nodes are the results of objective functions. In addition, minimum mission requirements of the optimization problem, which are given in Table 4.3, are also applied to these output nodes. The last output node, Empty Weight, is connected in order to monitor the empty weight of the aircraft. After all of the input and output nodes are added into the ModeFRONTIER software, Scheduler Node is added in order to determine Design of Experiments (DOE) properties, and optimization algorithm. Full Factorial is preferred for DOE and Multi Objective Genetic Algorithm (MOGA) is preferred for the optimization algorithm. Finally, the flowchart showing the optimization methodology, which is given in Figure 4.6, is built up for the optimization problem. The results for the variables strongly depend on the optimization methodology. Thus, the methodology, which is being used with the optimization driver, is very important to obtain the optimum design. More, the Design of Experiments (DOE) node and optimization algorithm are considered carefully before starting the optimization process.

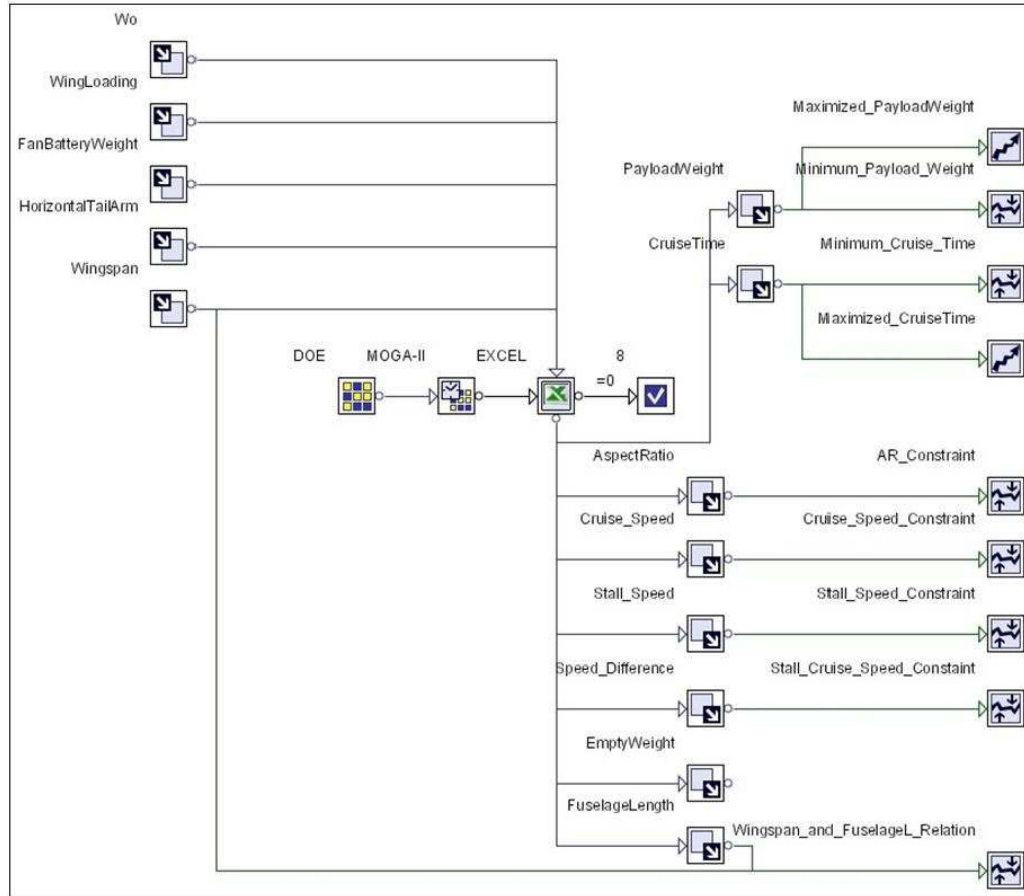


Figure 4.6 : Flowchart for the optimization problem

4.4.4.1 Design of Experiments (DOE)

An important step in an optimization process is the initial sampling of the design space. Design Of Experiments (DOE) originated in 1920 by a British scientist, Sir R. A. Fisher, as a method to maximize the knowledge gained from experimental data[17]. The traditional approach is to test one factor at a time (OFAT). The first factor is moved while the other factors are held constant, then the next factor is examined, and so on. Design of Experiments (DOE) provides a strong and universal framework to design and analyze all comparative experiments. With OFAT many runs are usually needed to get sufficient information and this is generally prohibitive. The DOE approach is in direct contrast to OFAT because it considers all factors simultaneously. With design of experiments, the best factor settings are used for obtaining a certain amount of information. The DOE Node is the starting node for any modeFRONTIER project, and is used to define the Design of Experiments algorithm to be used to create the initial set of designs to be evaluated. Accordingly,

one, and only one, such node must exist in any legal Work Flow. This node always appears in conjunction with the scheduler node, which actually determines which DOE designs will be evaluated. Full factorial algorithm, which is discussed in detail as follows, is decided to be used as DOE for the multi objective, multi disciplinary design optimization of the unmanned tailsitter aircraft.

4.4.4.2 Full Factorial

The Full Factorial algorithm generates every possible combination of all the parameters. A common full factorial is one with all input variables set at each two levels (lower bound and upper bound). A design with all possible lower and upper combinations of all the input variables is called a "full factorial design in two levels".

The number of total experiments is given as follows, where n_i is the number of levels for i^{th} variable and k the number of variables.

$$N = \sum_{i=1}^k n_i \quad (4.34)$$

The diagram of 3 levels of 3 variables, which results 27 experiments, is given as Figure 4.7. This full factorial allows the computation of 2nd order interactions.

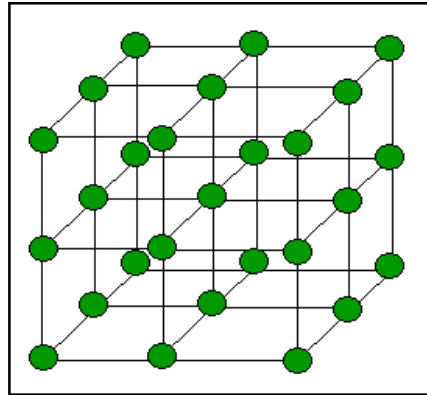


Figure 4.7 : Full factorial for 3 levels of 3 variables (27 experiments)

There are three ways to solve the above problem:

1. Reduce the number of levels for each variable, e.g., reduce n_i to 2 levels.
2. Reduce the number of variables.

For each variable the number of levels has to be defined. The level must be an integer equal or greater than 2. Even if the number of total designs is greater, the

maximum number of experiments generated with this algorithm is limited to 64000. This algorithm allows the estimation of how each variable affects the responses. The disadvantage of this method is that the number of experiments grows dramatically with the number of variables. A full factorial is practical when less than five or six input variables are being analyzed. With more than five or six input variables, testing all combinations becomes too hard. Full Factorial method works best with less than 8 variables and less than 4 levels. For each design variable the number of levels can be defined. The maximum number of generated designs is limited to 256000. Factorial levels are given in Table 4.5;

Table 4.5 : Full Factorial Levels of the Optimization Problem

Input Variable	Levels
W_0	3
Wing Loading	3
Wing Span	3
Horizontal Tail Arm	3
Fan Battery Weight	3

As seen from the table given above, “ $3^5 = 243$ Design of Experiments (DOE)” is going to be obtained for the design optimization of unmanned tailsitter aircraft. The full factorial levels for the design variables can not be increased any more since the number of DOE increases exponentially with an increment of levels. The increment of DOE increases the number of computations, and therefore the optimization time. For a good optimization, the correlation between the design variables should be low as shown in the right side of Figure 4.8. If the combinations are all in the same part of design space, the correlation between them is high as shown in the left side of the same figure. The set of good designs is well-distributed in space and not correlated.

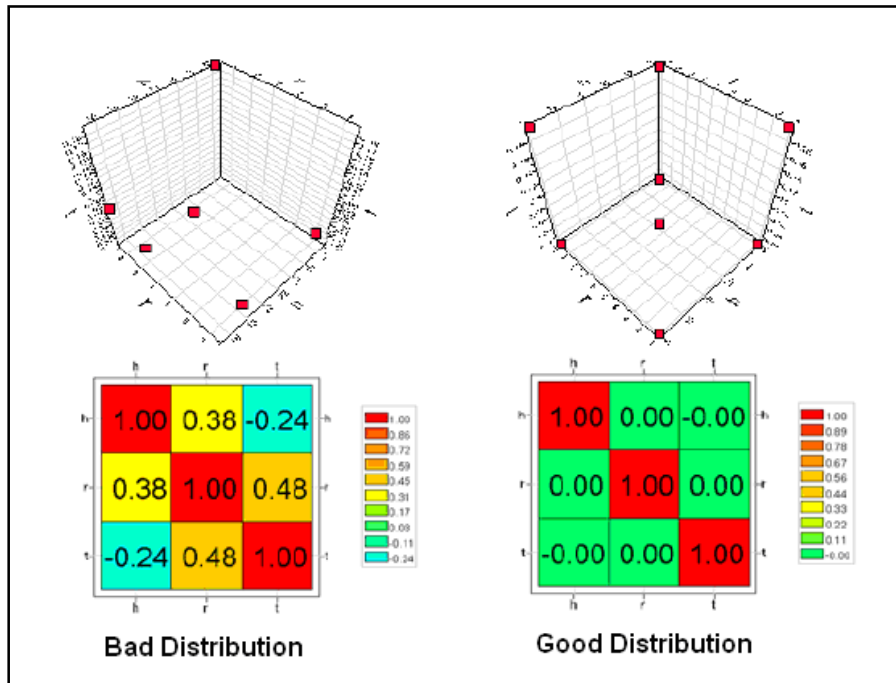


Figure 4.8 : Bad and Good Distribution of Correlation Matrix on DOE Table

For the design optimization of the unmanned tailsitter aircraft, the correlation between the variables is obtained as low as it might be due to using Full Factorial algorithm. Therefore, it can be stated that, the distribution of correlation matrix on Doe table is good as shown in Figure 4.9 given below:

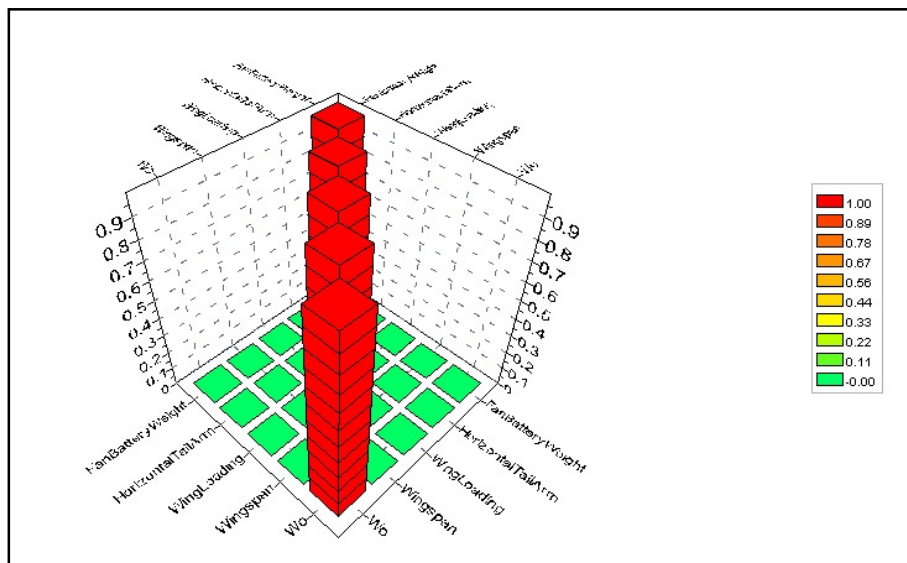


Figure 4.9 : Distribution of Correlation Matrix on DOE Table

It is obvious on Figure 4.9 that, the variables of the optimization problem are not too much related to each other; and therefore, the correlation matrix on DOE table is

well-distributed. The table form of distribution of correlation matrix on DOE table is given in Table 4.6:

Table 4.6 : Table of Distribution of Correlation Matrix on DOE Table

	W_0	Wing Span	Wing Loading	Horizontal Tail Arm	Fan Battery Weight
W_0	1	0	0	0	0
Wing Span	0	1	0	0	0
Wing Loading	0	0	1	0	0
Horizontal Tail Arm	0	0	0	1	0
Fan Battery Weight	0	0	0	0	1

4.4.4.3 Multi Objective Genetic Algorithm II (MOGA-II)

Main features of Multi Objective Genetic Algorithm II (MOGA-II) designed for fast Pareto convergence are listed below:

- 1) Supports geographical selection and directional cross-over
- 2) Implements Elitism for multiobjective search.
- 3) Enforces user defined constraints by objective function penalization.
- 4) Allows Generational or Steady State evolution.
- 5) Allows concurrent evaluation of independent individuals.

The number of individuals entries in the DOE table, N , are used as the problem's initial population. MOGA-II is an efficient multi-objective genetic algorithm (MOGA) that uses a smart multisearch elitism. This new elitism operator is able to preserve some excellent solutions without bringing premature convergence to local optimal fronts[17].

For simplicity, MOGA-II requires only very few user-provided parameters, several other parameters are internally settled in order to provide robustness and efficiency to the optimizer. The algorithm will attempt a number of evaluation equal to the size

of the loaded Design of Experiment (the initial population for the MOGA-II algorithm) multiplied by the number of generation. The size of the run is usually defined by the computing resources available. A rule of thumb would suggest possibly to accumulate an initial DOE of at least 16 design configuration and more than; “ $2 \times \text{number of variables} \times \text{number of objectives}$ ”.

The system will always check if one design evaluation has been already performed and will eventually skip the computation.

4.4.4.4 Genetic Algorithm

Many practical optimum design problems are characterized by mixed continuous-discrete variables, and discontinuous and nonconvex design spaces. If standard nonlinear programming techniques are used for this type of problem they will be inefficient, computationally expensive, and in most cases, find a relative optimum that is closest to the starting point. Genetic Algorithms (GAs) are well suited for solving such problems, and in most cases they can find the global optimum solution with a high probability. Although GAs were first presented systematically by Holland, the basic ideas of analysis and design based on the concepts of biological evolution can be found in the work of Rechenberg. Philosophically, GAs are based on Darwin's theory of survival of the fittest[18,19].

Genetic algorithms are based on the principles of natural genetics and natural selection. The basic elements of natural genetics-reproduction, crossover, and mutation are used in the genetic search procedure. GAs differ from the traditional methods of optimization in the following respects[19]:

1. A population of points (trial design vectors) is used for starting the procedure instead of a single design point. If the number of design variables is n , usually the size of the population is taken as $2n$ to An . Since several points are used as candidate solutions, GAs are less likely to get trapped at a local optimum.
2. GAs use only the values of the objective function. The derivatives are not used in the search procedure.
3. In GAs, the design variables are represented as strings of binary variables that correspond to the chromosomes in natural genetics. Thus the search

method is naturally applicable for solving discrete and integer programming problems. For continuous design variables, the string length can be varied to achieve any desired resolution.

4. The objective function value corresponding to a design vector plays the role of fitness in natural genetics.
5. In every new generation, a new set of strings is produced by using randomized parents selection and crossover from the old generation (old set of strings). Although randomized, GAs are not simple random search techniques. They efficiently explore the new combinations with the available knowledge to find a new generation with better fitness or objective function value.

Genetic Algorithms have been used in several engineering problems with clear advantages over other traditional algorithms. The major advantages of these techniques are mainly related to robustness of the procedure. In simple GA applications a large number of fitness evaluation is needed to reach a satisfactory solution[17].

With the continuing growth of computing resources available, the engineers' attention has modified the role of complex simulation that is more and more used directly in the design process. This aspect has also underlined the substantial weakness of traditional optimization approaches that can usually produce only single-objective optimized solution and only if the objective function satisfies continuity and often derivability conditions. This fact together with the need of multidisciplinary approach to design caused a growing interest into the use of Genetic Algorithms as general purpose optimizers. A large number of examples of engineering application can in fact be found in the literature.

Most real-life design procedures are complex tasks that have to deal with multidisciplinary environments, not always clearly defined targets, constraints to be satisfied. In this sense even though the target of the optimization could be expressed with a single expression like: "do the best possible design", the optimization process must consider several different usually conflicting objectives and the compromise obtainable might not be a-priori known. The possibility of looking not only for a single good solution but for a set of solutions (called the "Pareto Set"), that satisfy

different levels of compromise might be of great help to the decision maker that must select the most suitable one.

Three main issues listed below, make GAs more attractive and maybe unique among the aerodynamic design optimization methods:

- ☆ GAs are usually much more robust than gradient based algorithm and can tolerate even approximate or noisy design objectives evaluation,
- ☆ GA can be efficiently parallelized and can therefore take full advantages of the massively parallel computer architecture,
- ☆ GA can directly approach a multi-objective optimization problem.

It must be noted however that the main concern related to the use of Genetic Algorithm for engineering problems involving the use of complex simulation codes is the computational effort needed for the accurate evaluation of a design configuration that, in the case of a crude application of the technique, might leads to unacceptable computer time if compared with other more classical algorithms. With the help of parallel supercomputers and considering the fact that the computational performances of available machines is continuously growing, this problem at first glance might seem to be solvable by the computer technology development. However it is also known that the most powerful today available computer is still far from having sufficient performance even for single "multiphysics" simulation and therefore any effort in the direction of computational cost reduction of the optimization process should be seen at least as an opportunity to face more challenging design problems. Though genetic algorithm has many advantages to the classical optimization techniques, it also has some disadvantages. GA does not guarantee that the result of the optimization process is the optimum solution. Moreover, the result of the optimization process is obtained by statistically, and GA does not give the possibility of the solution. The first reason to prefer genetic algorithm for the considered optimization problem is being suitable to multi-objective optimization problems. When the optimization problem has complex objective functions consisting of many variables, similar to the optimization problem of ITU – BYU Tailsitter UAV, the possibility of finding local minima instead of global minima increases. Therefore, GA, which is more successful than the other algorithms in determining global minima, is more suitable for the optimization problem. In addition, using only the results of objective function, makes GA one step

further. Obtaining a new design as a result of each genetic algorithm step allows observing the alternative solutions which is important to design a competitive tailsitter UAV.

4.4.4.5 Genetic Algorithm for Multi-Objective Optimization

Genetic algorithm discussed in the previous section, is now ready to be considered for multi-objective optimization. The multi-objective optimization problem can be expressed as follow [17].

$$\begin{aligned} \max F_i(\bar{x}), \text{ for } i=1,n \\ g_j \leq 0, \text{ for } j=1,m \end{aligned} \quad (4.35)$$

It is obvious that in general the solution is not unique if the functions are not linearly dependent. With the introduction of the Pareto dominance concept, it is possible to divide any group of solutions into two subgroups: the "dominated" and the "non-dominated" one. Solutions belonging to the second group are the "efficient" solutions, i.e. the ones for which it is not possible to increase any objective value without deteriorating the values of the remaining objectives. In more formal terms and in the case of maximization problems it is possible to say that the solution \bar{x} dominates \bar{y} if the following relation is true:

$$\bar{x} >_p \bar{y} \Leftrightarrow (\forall i \ F_i(\bar{x}) \geq F_i(\bar{y})) \cap (\exists j \ F_j(\bar{x}) > F_j(\bar{y})) \quad (4.36)$$

Classical optimization algorithms are capable, under strict continuity and derivability hypothesis, of finding the optimal value only in the single objective case and therefore the problem of finding the group of non dominated solutions (the Pareto Set) is reduced to several single objective optimization where the objective becomes a weighted combination of the objectives called utility function "Obj", given as Equation-4.4, where \bar{x} is the vector of variables and W_i are the weights for the objectives F_i :

$$Obj = \sum_{i=1}^n W_{ik} F_i(\bar{x}) \quad (4.37)$$

A more sophisticated and effective way to transform a multi-objective problem into a single-objective problem is the use of an Utility Function that is not a simple

weighted sum of objectives but that is a non-linear combination of the objectives, i.e. the weights are not constant but are given as a monotone function of the objective value as necessary when comparing objectives of totally different nature like cost and performances.

While traditional optimization algorithm do need the use of an utility function, the particular structure of GA can face the multi-objective optimization problem in a more direct way developing populations in which the diversities follow the conflicting objectives.

5. OPTIMIZATION PROCESS

After the optimization problem is considered in detail, and the optimization methodology is discussed with great care, optimization process become ready to be carried out. Previously discussed objective functions, side constraints and design variables are applied to the Esteco modeFRONTIER and Microsoft Excel softwares as previously considered. Noting that, Full Factorial DOE node and MOGA-II algorithm are used for optimization process. When the flowchart, which is previously given in Figure-4.1, is ran the total number of 13550 designs is obtained. The total design points are consisting of feasible designs, unfeasible designs and errors. Feasible designs are the design points with all the constraints are satisfied, while unfeasible designs consist of the design points with at least one unsatisfied constraint. The errors are the designs with indefinite design points. The distribution of feasible, unfeasible design points and errors is shown within the chart given as Figure-5.1. It can be stated that, the optimization methodology is correctly selected according to the distribution of obtained design points. The design summary is given in Table-5.1 below and then all of the design points obtained for the optimization problem are shown in Figure-5.2 as follows:

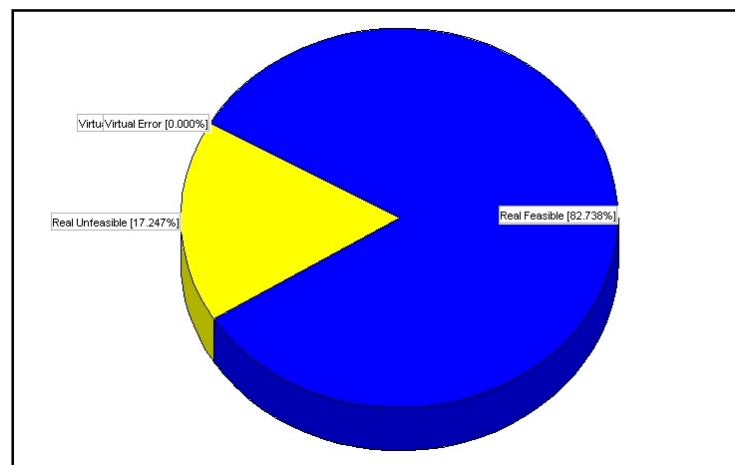
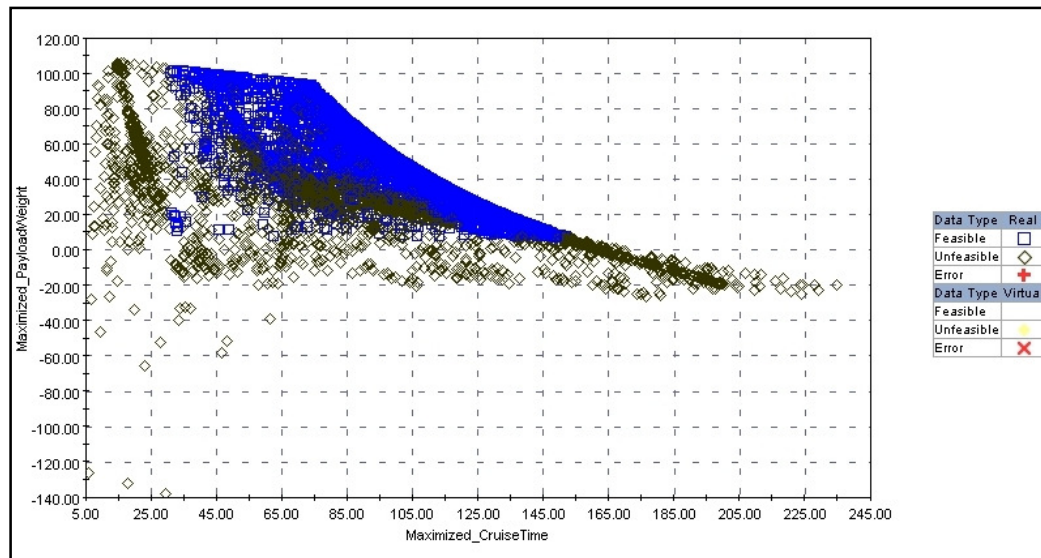


Figure 5.1 : Design summary chart of the optimization problem

Table 5.1 : Design summary of the optimization problem

Designs	Number
Total Design	13550
Feasible Design	11211
Unfeasible Design	2337
Errors	2

**Figure 5.2 :** All design points for the optimization problem

As previously stated, the design points with at least one broken constraint are the unfeasible design points. For the optimization problem 3 of the constraints are strictly satisfied, while the other 4 of the constraints are not satisfied at 2337 design points. The number of broken constraints is listed in Table 5.2. For some of the design points more than one design constraint is broken. Therefore, the total number of broken constraints is more than the number of unfeasible design points. Aspect ratio constraint is the most broken constraint while stall speed, stall speed-cruise speed relation and cruise speed constraints are never broken by the design points. The distribution of the broken constraints is given in Figure 5.3 as pie chart.

Table 5.2 : Broken constraints at unfeasible design points

Constraints		Broken Constraints
Wingspan-Fuselage Length Relation	$b \geq l_{fuselage}$	981
Stall Speed	$V_{stall} < 30m/s$	0
Stall Speed-Cruise Speed Relation	$V_{cruise} - V_{stall} > 3m/s$	0
Cruise Speed	$V_{cruise} \leq 50m/s$	0
Aspect Ratio	$AR \geq 4$	1473
Cruise Time	$t_{cruise} \geq 30min$	380
Payload Weight	$W_{payload} \geq 8N$	731

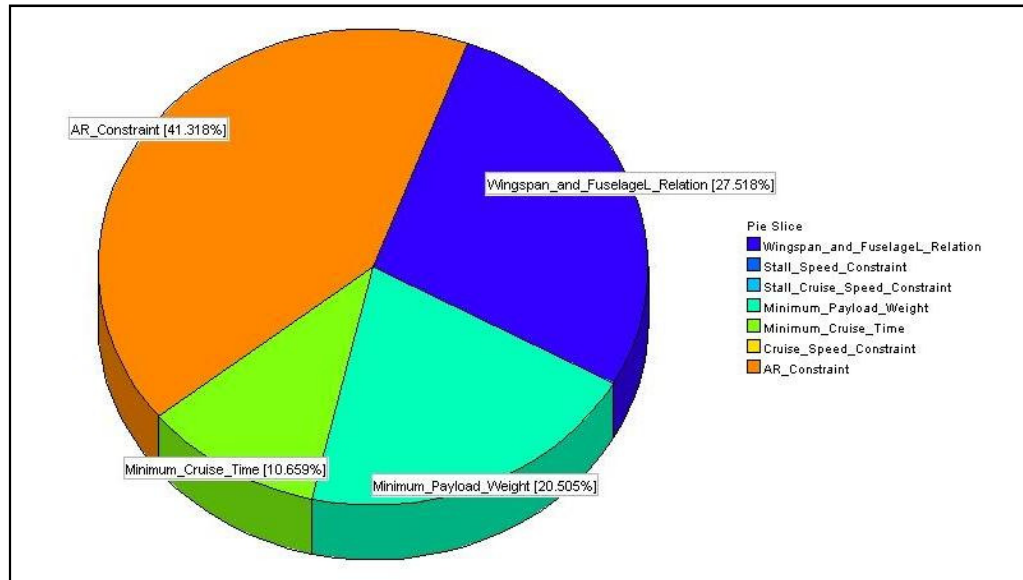


Figure 5.3 : Chart of broken constraints at unfeasible design points

For the optimization process, feasible design points must be evaluated in detail. The feasible design points obtained for the multiobjective-multidisciplinary design optimization of unmanned tailsitter aircraft is shown in Figure 5.4.

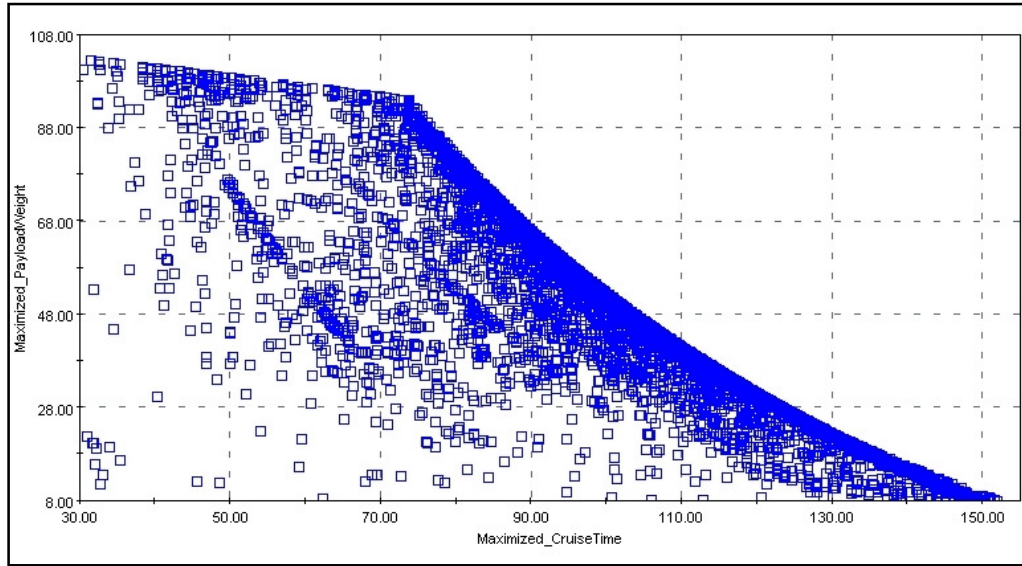


Figure 5.4 : Feasible design points for the optimization problem

As seen from the figure given above, there are 11211 fully distributed feasible design points obtained as a result of optimization. Due to having a multiobjective optimization problem, the design point both having maximized payload weight and cruise time must be determined. Therefore, Pareto Chart is used in order to determine the set of optimal solutions. In Figure 5.5, Pareto Chart which consists of 3021 optimum design points for objective functions is given.

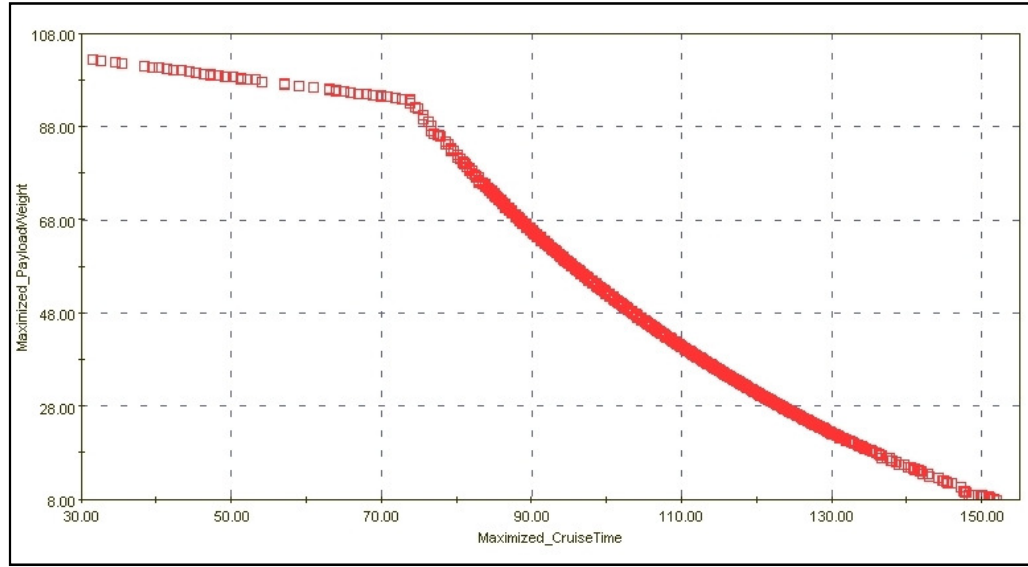


Figure 5.5 : Pareto chart for optimum design points

After all the pareto design points are examined in detail, following figures are obtained with the help of modeFRONTIER. The figures show the frequencies of the design variables and objective functions. It can be stated according to the figures that, frequency distributions of maximum takeoff weight and horizontal tail arm are normal distributions. Additionally, the distributions of objective functions, payload weight and cruise time, are also normal distributions. However, the distributions of wing loading, wing span and fan battery weight are different from the normal distribution. According to Figure 5.7, nearly 90 % of the pareto designs have wing loading of more than 190 N/m^2 . Next, According to Figure 5.8, nearly all of the pareto designs have wing span of 2 m which is also the upper limit of wing span constraint. Therefore, it can be stated that, wing span constraint limits the pareto designs. According to Figure 5.10, nearly all of the pareto designs have battery weight of 15 N which is also upper limit of battery weight constraint. Therefore, similar to wing span constraint, it can be stated that battery weight constraint limits the pareto designs.

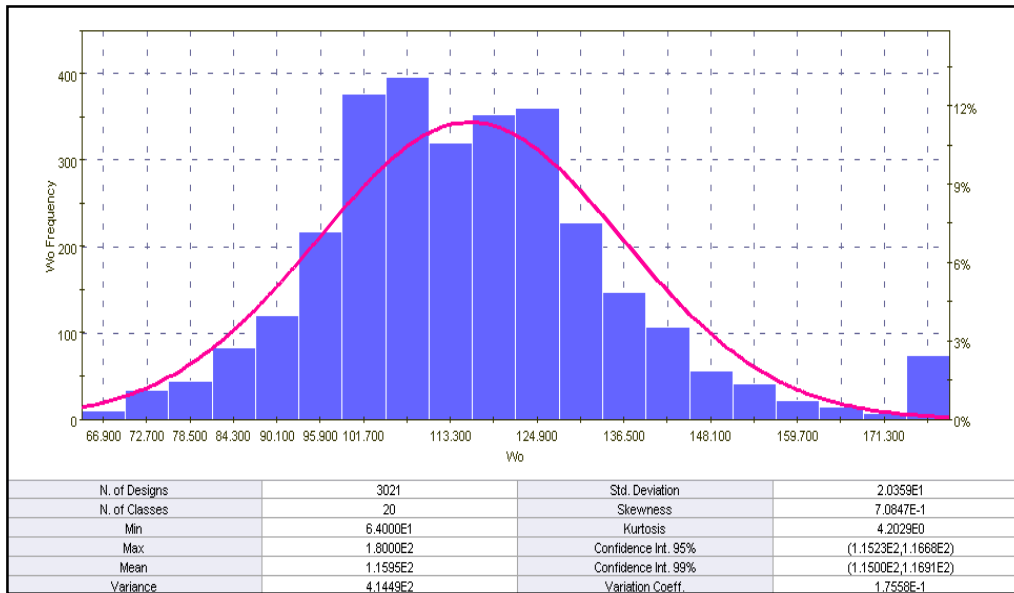


Figure 5.6 : Frequency histogram for maximum takeoff weight of pareto design points

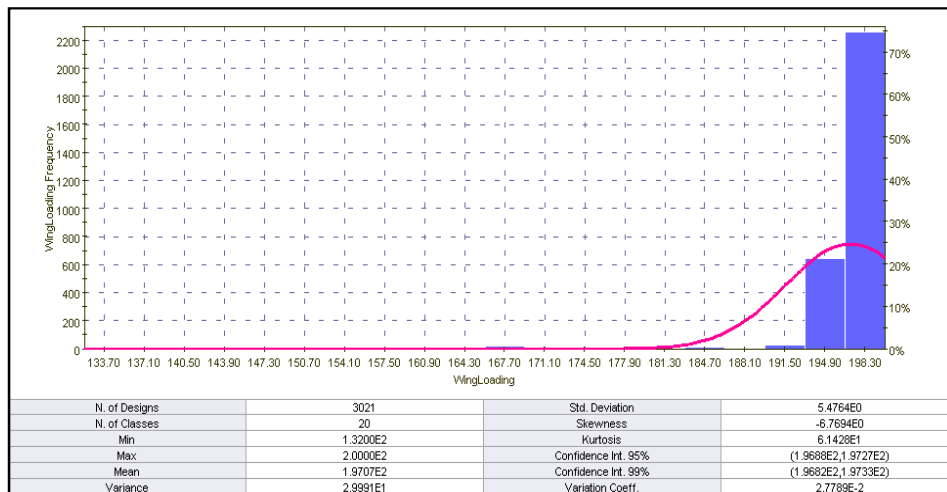


Figure 5.7 : Frequency histogram for wing loading of pareto design points

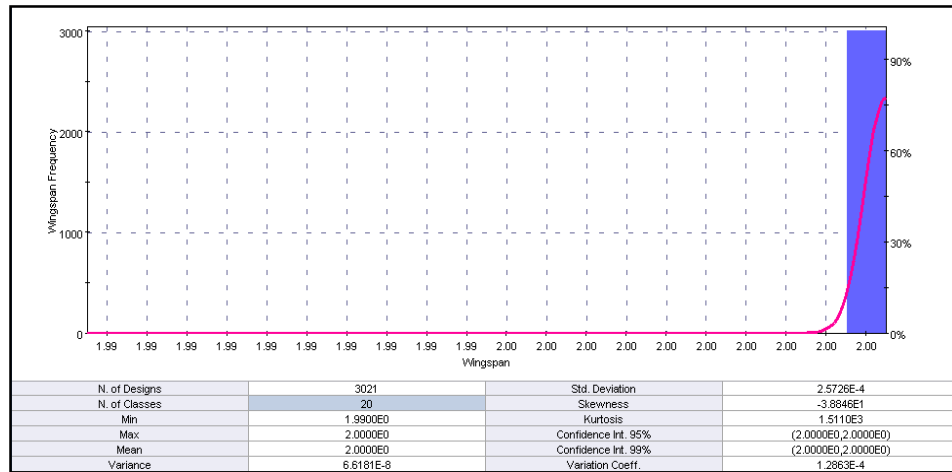


Figure 5.8 : Frequency histogram for wingspan of pareto design points

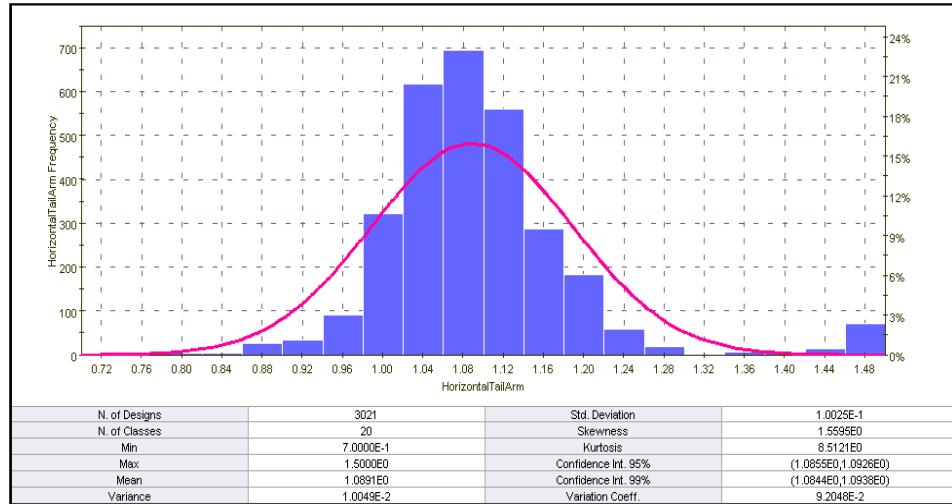


Figure 5.9 : Frequency histogram for horizontal tail arm of pareto design points

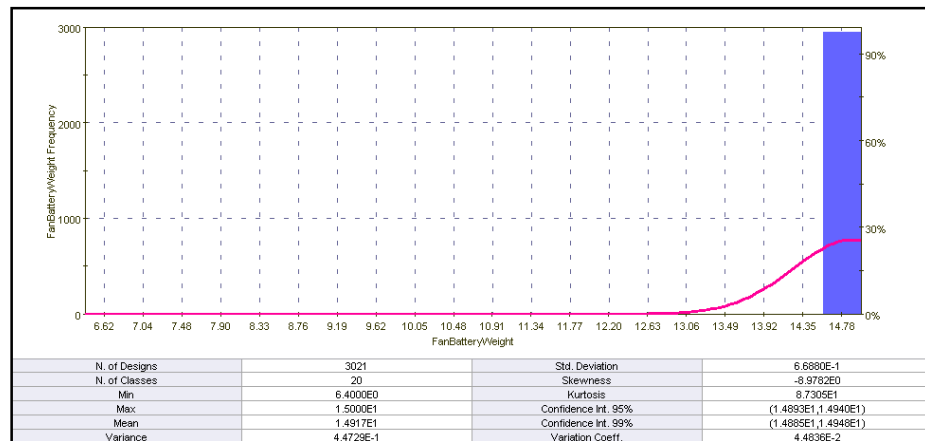


Figure-5.10: Frequency histogram for fan battery weight of pareto design points

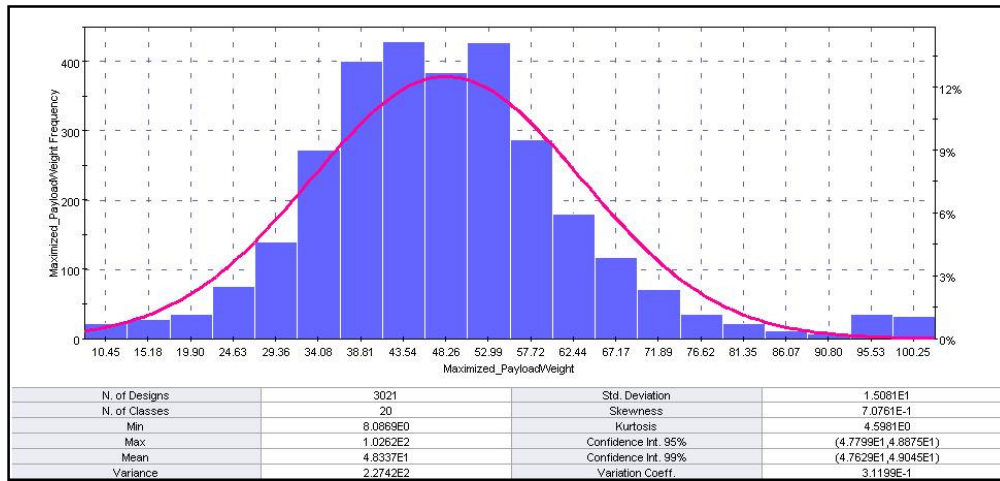


Figure-5.11: Frequency histogram for payload weight of pareto design points

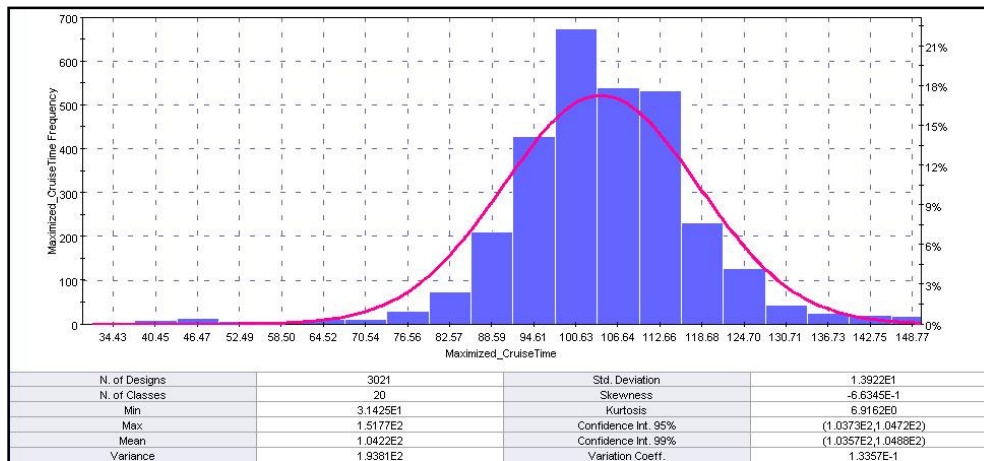


Figure-5.12: Frequency histogram for cruise time of pareto design points

Considering the Pareto Chart given in Figure 5.5; the design points with better (maximized) values of both objective functions, is pointed as shown in Figure 5.13. Due to the severe variation of design points over the selected design set, the optimum design point is considered within this design set. By the way the design points having optimum points only for one objective function is eliminated. The optimum design points for the selected design set, shown in Figure 5.13, are listed in Table 5.3 given as follows:



Figure 5.13 : Selected design set from the pareto chart

As previously stated, the severe variation of the pareto chart should consist of optimum design point. Therefore the design point, with ID: 2478 shown in Figure-5.14, at the corner of the chart is decided to be the real design point for the multiobjective-multidisciplinary design optimization of unmanned tailsitter aircraft. The comparison of the initial design and the optimum design is summarized in Table 5.4. As a result of the optimization, initial MTOW is increased from 56.2 N to 178 N, which is nearly 3 times the initial value. Moreover, maximum payload capacity is increased from 13.5 N to 92.39 N, which is nearly 7 times of the initial value and therefore it is a good optimized value. Additionally, fan battery weight is increased to 15 N and by the help of this increment cruise time is changed from 40 min to 74.37 min which is also another good optimization result.

Table 5.3 : Design points of dominant design set

Design ID	W_0 (N)	W / S (N/m ²)	b (m)	l_{HT} (m)	$W_{fanbattery}$ (N)	$W_{payload}$ (N)	t_{cruise} (min)
242	180	200	2	1.50	15.0	94.02	73.65
594	180	200	2	1.48	15.0	93.98	73.66
1642	172	200	2	1.50	15.0	88.52	76.50
1653	180	200	2	1.50	14.4	94.62	70.71
1768	180	200	2	1.50	14.8	94.22	72.67
2159	180	200	2	1.41	15.0	93.82	73.67
2478	178	200	2	1.38	15.0	92.39	74.37
3349	177	200	2	1.50	15.0	91.96	74.70
3428	173	200	2	1.44	15.0	89.13	76.15
3613	180	200	2	1.45	14.4	94.52	70.72
4221	180	200	2	1.23	15.0	93.11	73.68
4698	175	199	2	1.25	15.0	89.72	75.44
4898	180	200	2	1.49	15.0	94.00	73.66
6219	175	200	2	1.50	15.0	90.59	75.41
6746	180	200	2	1.40	15.0	93.80	73.68
7089	180	200	2	1.46	15.0	93.94	73.66
7159	180	200	2	1.46	14.4	94.54	70.72
7222	173	200	2	1.50	15.0	89.21	76.13
7708	180	199	2	1.50	14.6	94.24	71.68

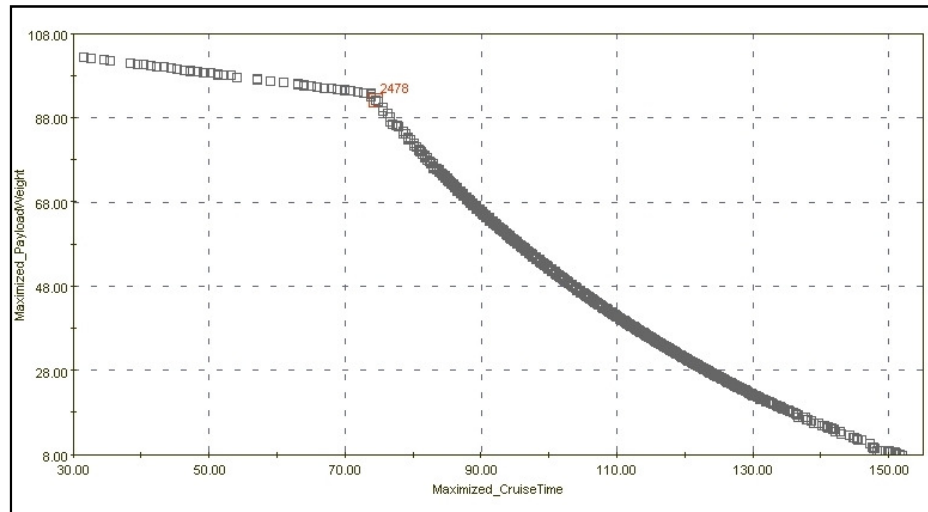


Figure 5.14 : Selected design point as optimum design point

Table 5.4 : Comparison of initial design and selected design (ID:2478)

Parameters	Initial Design	Selected Design
W_0 (N)	56.2	178
Wing Loading (N/m^2)	200	200
Wingspan (m)	1.3	2
Horizontal Tail Arm(m)	0.78	1.38
FanBattery Weight(N)	4.76	15
Payload Weight (N)	13.5	92.39
Cruise Time (min)	40	74.37
Aspect Ratio	6	4.49
Fuselage Length (m)	1.2	1.86
Cruise Speed (m/s)	22.1	30.87
Stall Speed (m/s)	16.81	16.81
Empty Weight (N)	15.73	36.73
Wing Area (m^2)	0.28	0.89

6. WIND TUNNEL TESTS

In order to quantify the thrust output and the power consumption of the selected propulsion systems, some wind tunnel test were conducted. However, because of the size restrictions of the wind tunnel in Istanbul Technical University, propeller propulsion system test could not be done. On the other hand, EDF propulsion tests have been completed successfully and the test data has been collected.

First of all, a test bed for EDF propulsion system has been build and seen in Figure 6.1:

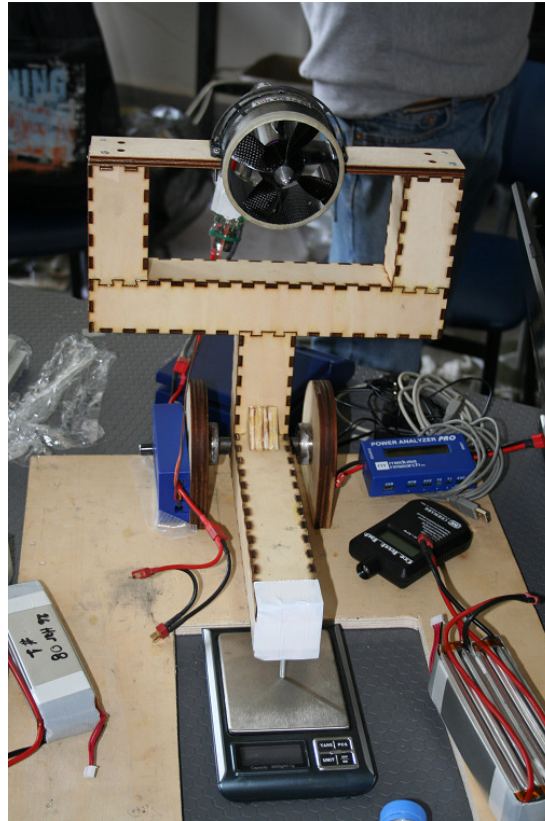


Figure 6.1 : EDF and testbench system.

To collect the required parameters from wind tunnel test, optical tachometer, digital scale and watt meter are set up for measuring rotation per minute, thrust and power, respectively. The complete test setup is shown in Figure 6.2:

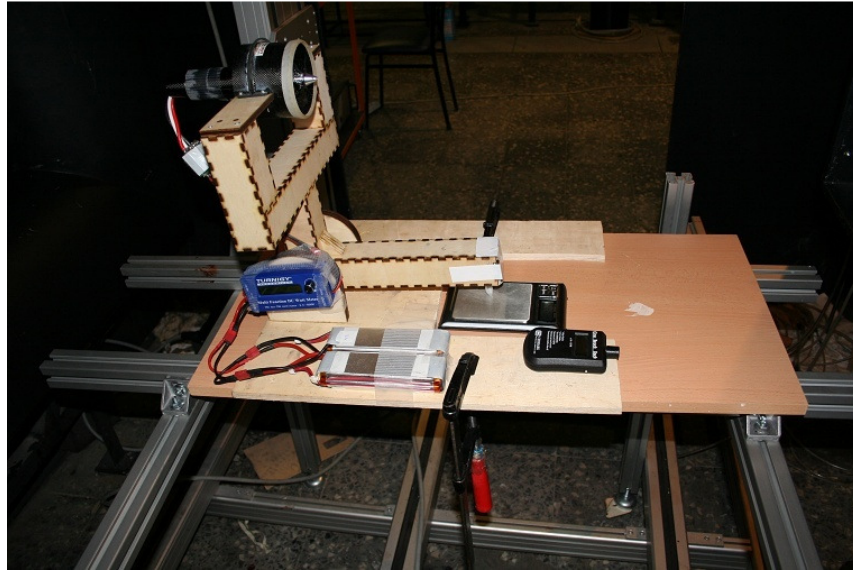


Figure 6.2 : Wind tunnel test setup for EDF propulsion system

Wind tunnel tests have been performed under several wind speed and RPM conditions to reach different advance ratio values. After completing wind tunnel test, the obtained data with graphic is given in Figure 6.3:

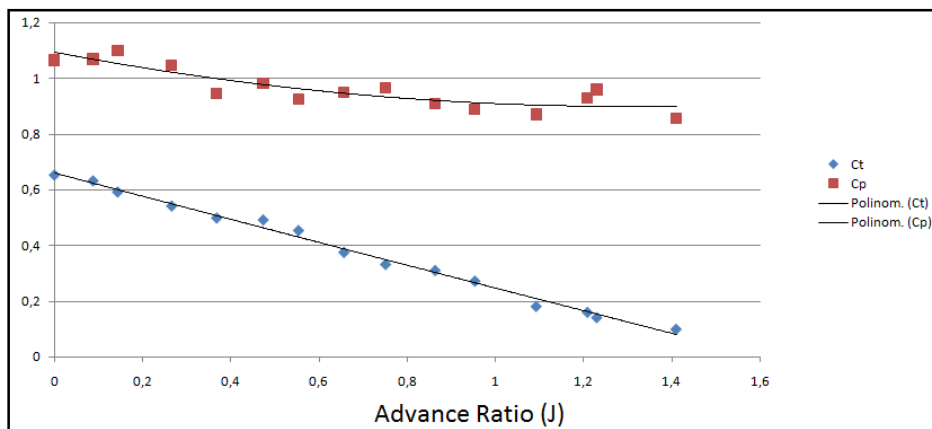


Figure 6.3 : Graphical representation of the obtained wind tunnel data

7. VORTEX-LATTICE ANALYSIS

Vortex lattice method (VLM) is a numerical CFD method that is widely used in preliminary design of aircraft. VLMs can compute the air/gas flow around a wing or any aerodynamic surface. More, it is based on the potential flow theory, in which the viscous effects are neglected. Turbulence and boundary layers are not resolved with this method. On the other hand, besides all the incapacities of the method, induced drag, lift and basic aerodynamic derivatives can be calculated with high level of accuracy when comparing with the wind tunnel data [20].

As software, there are several open source VLM solvers, that can be found on internet. Therefore, because of the ease of user interface and accuracy, TORNADO software is selected for analyzing ITU Tailsitter UAV. Tornado is an improved VLM method, which is being developed as a collaboration between KTH, Royal institute of Technology in Stockholm Sweden and University of Bristol, United Kingdom and the University of Linköping. First, MATLAB code of TORNADO software is run under MATLAB software. As second step, aircraft fuselage, wings and stabilizers are modeled with the help of the user interface of the software. After initializing the conditions like solver type, wind speed, angle of attack etc., the software gives a graphical output to the user. In ITU Tailsitter design, the outputs is seen in Figure 7.1, 7.2, 7.3 and 7.4:

TORNADO CALCULATION RESULTS, Central difference, RUDDER DERIVs					
JID:	test				
Reference area:	0.89	α :	0	P:	0
Reference chord:	0.47855	β :	0	Q:	0
Reference span:	2.000	Airspeed:	29	R:	0
CL_δ	1.9657	CD_δ	0.059935	CY_δ	-1.6808e-011
	-7.6589e-007		1.2867e-006		-0.042286
	0.34759		0.001707		-7.7515e-012
Cl_δ	1.3957e-012	Cm_δ	-1.7737	Cn_δ	-1.4401e-011
	0.0028615		2.3614e-006		-0.036991
	5.1494e-013		-0.85175		-6.683e-012

Figure 7.1 : Derivative calculations by TORNADO code

TORNADO CALCULATION RESULTS, Derivatives					
JID:	test				
Reference area:	0.89	α :	0	P:	0
Reference chord:	0.47855	β :	0	Q:	0
Reference span:	2.000	Airspeed:	29	R:	0
CL derivatives :		CD derivatives :		CY derivatives :	
CL_α	3.7412	CD_α	0.09756	CY_α	9.9937e-011
CL_β	-1.0439e-005	CD_β	4.2993e-006	CY_β	-0.10973
CL_P	9.3343e-009	CD_P	6.2608e-007	CY_P	-0.017771
CL_Q	10.3763	CD_Q	0.23393	CY_Q	7.4657e-010
CL_R	-1.144e-007	CD_R	3.658e-007	CY_R	-0.19861
Roll derivatives :		Pitch derivatives :		Yaw derivatives :	
Cl_α	-6.5819e-012	Cm_α	-3.6065	Cn_α	8.5144e-011
Cl_β	-0.016065	Cm_β	1.2827e-005	Cn_β	-0.09244
Cl_P	-0.34237	Cm_P	-2.8454e-008	Cn_P	0.0041021
Cl_Q	-1.7502e-011	Cm_Q	-12.1942	Cn_Q	6.3502e-010
Cl_R	-0.0054334	Cm_R	3.1198e-007	Cn_R	-0.16889

Figure 7.2 : Derivative calculations by TORNADO code

Tornado Computation Results									
JID:	test	Downwash matrix condition: 289.8239							
Reference area:	0.89	α :	0	P:	0				
Reference chord:	0.47855	β :	0	Q:	0 0 0				
Reference span:	2.000	Airspeed:	29	R:	0 0 0				
Net Wind Forces: (N)			Net Body Forces: (N)			Net Body Moments: (Nm)			
Drag:	1.64665	X:	1.64665	Roll:	5.0705e-011				
Side:	-4.9688e-010	Y:	-4.9688e-010	Pitch:	-21.5915				
Lift:	184.8826	Z:	184.8826	Yaw:	-6.0598e-010				
CL	0.4017	CZ	0.4017	Cm	-0.18265				
CD	0.0026178	CX	0.0026178	Cn	-1.7179e-012				
CY	-2.0115e-012	CC	-2.0115e-012	Cl	1.4374e-013				
CD _{trefftz}	N/A								
STATE:									
alpha:	0	P:	0	0 0 0 0 0 0 0					
beta:	0	Q:	0	Rudder setting [deg]:	0 0 0 0 0 0 0				
Airspeed:	29	R:	0	0 0 0 0 0 0 0					
Altitude:	0	PG Correction:		0					
Density:	1.225								

Figure 7.3 : Aerodynamic force calculations by TORNADO code

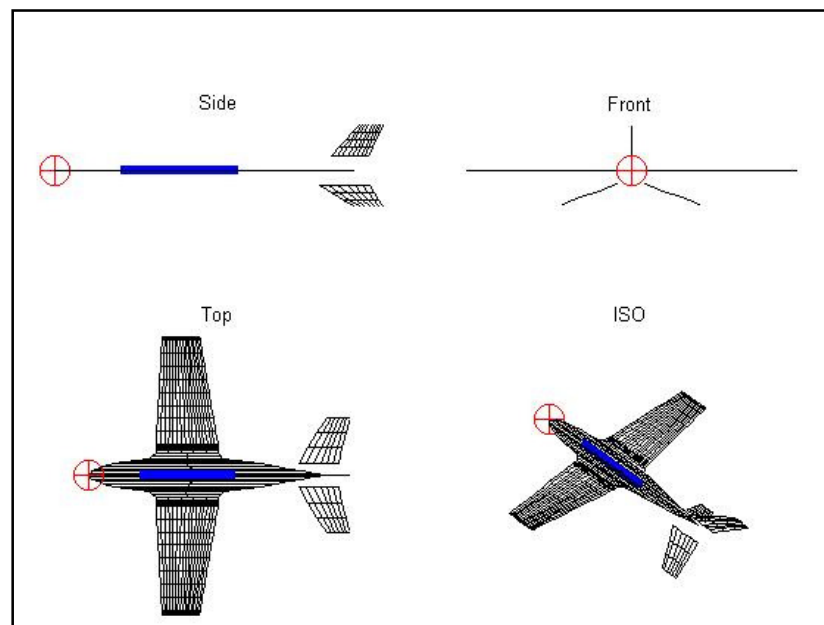


Figure 7.4 : Graphical output of the given sizing data

8. LONGITUDINAL STATIC STABILITY ANALYSIS

Longitudinal static stability is the stability of an aircraft around pitch axis during non-changing or static flight conditions. Moreover, longitudinal static stability analysis shows whether an aircraft can fly or not within the desired handling qualities.

There are three types of stability conditions, which are going to be considered in static stability analysis. The first one is stable state. In this state, if an external forces apply on an airplane during equilibrium flight, the aircraft tends to restore its original speed and orientation, without any input. Second, in neutrally stable (zero stability) state, the pitch disturbant force causes nothing. Thus, the airplane remains its new pitch angle until the airspeed changes affect the stability condition of the airplane. Third is unstable state, in which the airplane cannot remain its position under any pitch disturbant force.

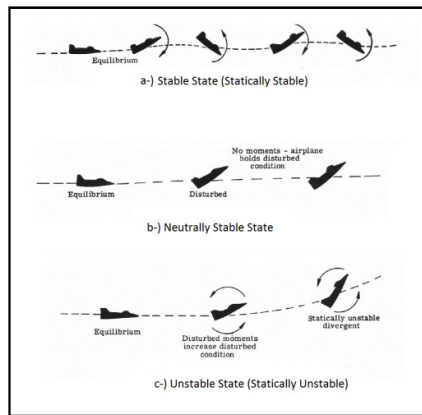


Figure 8.1 : Illustration of stable (a), neutrally stable (b) and unstable (c) states

As seen in Equation 8.1, to ensure the positive static stability, the angle of attack rate of change of airplane's moment should be smaller than zero; in other words, the pitching moment slope must have a negative slope.

$$\frac{dC_m}{d\alpha} < 0 \quad (8.1)$$

To make the longitudinal static stability analysis, neutral point and static margin must be determined.

8.2 Determination of Component Moments

The total pitching moment slope is the summation of the moment characteristics of the aerodynamic parts of the aircraft. These are generally wings, fuselage, horizontal tail, propulsion system and control surfaces.

8.3 Wing Contribution

Wing's contribution to an airplane's static stability can be understood with the help of Figure 8.2 shown below;

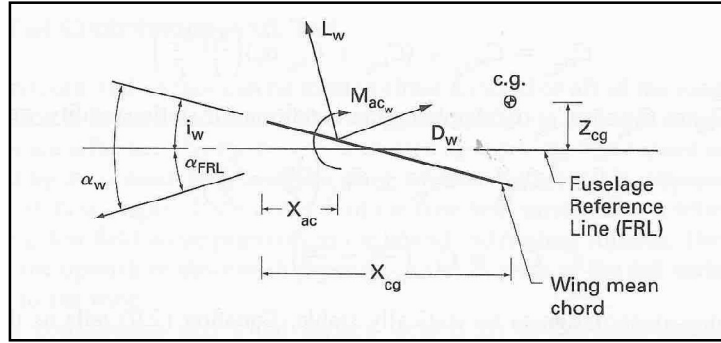


Figure 8.2 : Illustration of wing's contribution to the pitching moment

If we write down the summation of moments about the center of gravity, Equation 8.2 is obtained as below;

$$M_{cgw} = L_w \cdot \cos(\alpha_w - i_w) \cdot [X_{cg} - X_{ac}] + D_w \cdot \sin(\alpha_w - i_w) \cdot [X_{cg} - X_{ac}] \\ + L_w \cdot \sin(\alpha_w - i_w) \cdot [Z_{cg}] - D_w \cdot \cos(\alpha_w - i_w) \cdot [Z_{cg}] + M_{acw} \quad (8.2)$$

To undimensionalize the equation, we can divide the Equation 8.2 by Equation 8.3;

$$\frac{1}{2} \rho \cdot V^2 \cdot S \cdot \bar{c} \quad (8.3)$$

After dividing Equation 8.2 by 8.3, we can obtain a undimensionalized moment equation as seen below;

$$C_{m_{cgw}} = C_{L_w} \cdot \cos(\alpha_w - i_w) \cdot \left[\frac{X_{cg}}{\bar{c}} - \frac{X_{ac}}{\bar{c}} \right] + C_{D_w} \cdot \sin(\alpha_w - i_w) \cdot \left[\frac{X_{cg}}{\bar{c}} - \frac{X_{ac}}{\bar{c}} \right] \\ + C_{L_w} \cdot \sin(\alpha_w - i_w) \cdot \left[\frac{Z_{cg}}{\bar{c}} \right] - C_{D_w} \cdot \cos(\alpha_w - i_w) \cdot \left[\frac{Z_{cg}}{\bar{c}} \right] + C_{m_{acw}} \quad (8.4)$$

With some assumptions and approximations, Equation 8.4 can be simplified. These are;

$$\cos(\alpha_w - i_w) = 1 \quad (8.5)$$

$$\sin(\alpha_w - i_w) = \alpha_w - i_w \quad (8.6)$$

$$C_L \gg C_D \quad (8.7)$$

Moreover, the vertical component of center of gravity's location can be also be neglected. In this case, the simplified equation can be seen below;

$$C_{m_{cg_w}} = C_{m_{ac_w}} + C_{L_w} \cdot \left[\frac{X_{cg}}{\bar{c}} - \frac{X_{ac}}{\bar{c}} \right] \quad (8.8)$$

The open form of Equation 8.8 can be seen after writing down the wing's lift coefficient in terms of wing's lift curve slope and zero lift coefficient;

$$C_{m_{cg_w}} = C_{m_{ac_w}} + (C_{L_{0_w}} + C_{L_{\alpha_w}} \cdot \alpha_w) \cdot \left[\frac{X_{cg}}{\bar{c}} - \frac{X_{ac}}{\bar{c}} \right] \quad (8.9)$$

For static stability calculations, the variations of the equations 8.9 can also be written in Equation 8.10 and 8.11 respectively;

$$C_{m_{0_w}} = C_{m_{ac_w}} + C_{L_{0_w}} \cdot \left[\frac{X_{cg}}{\bar{c}} - \frac{X_{ac}}{\bar{c}} \right] \quad (8.10)$$

$$C_{m_{\alpha_w}} = C_{L_{\alpha_w}} \cdot \left[\frac{X_{cg}}{\bar{c}} - \frac{X_{ac}}{\bar{c}} \right] \quad (8.11)$$

If the design includes only wing as component, Equation 8.9 tells us that the aerodynamic center must be aft of the center of gravity to make the moment slope negative.

8.3.1 Tail Contribution

In this chapter, contribution of the horizontal tail to the airplane's moment will be discussed. In ITU Tailsitter design, horizontal tail is located behind the main wing. Therefore, the force and moment diagram can be drawn as seen in Figure 8.3;

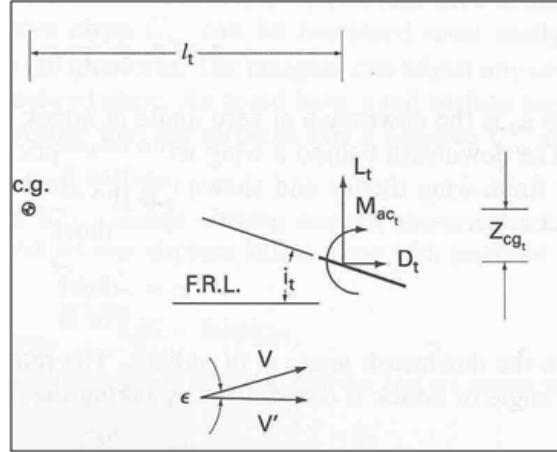


Figure 8.3 : Illustration of tail's contribution to the pitching moment

After making an assumption that the lift created by the tail is much more bigger than the drag created by the tail and according to Figure 8.3, the pitching moment created by the tail around the center of gravity can be written as below;

$$C_{m_{cg_t}} = \eta \cdot V_H C_{L_{\alpha_t}} \cdot [\epsilon_0 + i_w - i_t] - \eta \cdot V_H C_{L_{\alpha_t}} \cdot \alpha \left(1 - \frac{d\epsilon}{d\alpha}\right) \quad (8.12)$$

After implementing the linear expression for the pitching moment, which is seen in Equation 8.13; Equation 8.14 can be obtained;

$$C_{m_{cg_t}} = C_{m_0} + C_{m_{\alpha}} \cdot \alpha \quad (8.13)$$

$$C_{m_{\alpha_t}} = -\eta \cdot V_H C_{L_{\alpha_t}} \cdot \left(1 - \frac{d\epsilon}{d\alpha}\right) \quad (8.14)$$

8.3.2 Fuselage Contribution

In this chapter, the moment curve slope of the fuselage is determined by using Multhopp's method [21]. This methods determines the fuselage's moment curve slope in terms of its length, nose and tail angles, width and height. To write down the Multhopp's equation;

$$C_{m_{\alpha_f}} = \frac{1}{36.5.S.c} \sum_{x=0}^{x=l_f} w_f^2 \frac{\partial \epsilon_u}{\partial \alpha} \cdot \Delta x \quad (8.15)$$

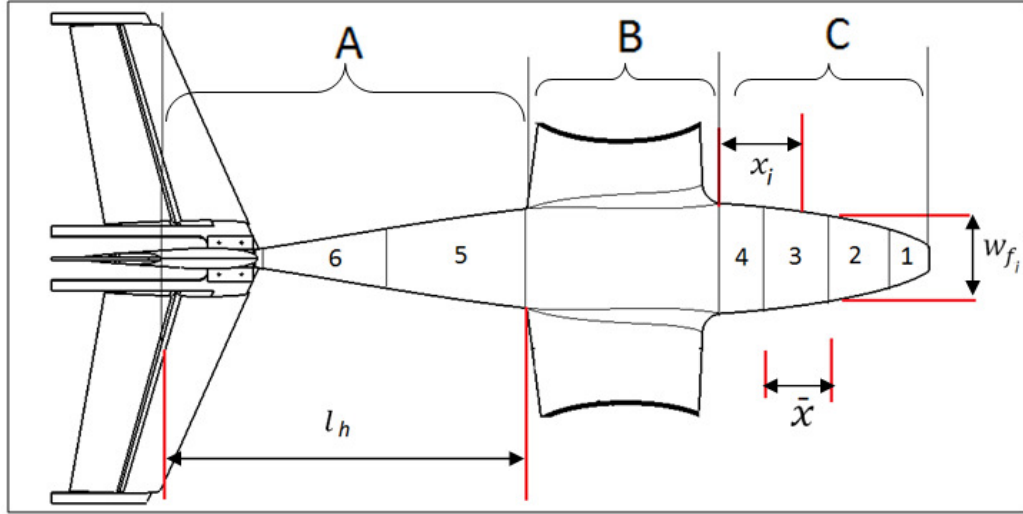


Figure 8.4 : Fuselage moment slope determination diagram

For region A in Figure 8.4, downwash slope ($\frac{\partial \epsilon_u}{\partial \alpha}$) is found with the help of Equation 8.15;

$$\frac{\partial \epsilon_u}{\partial \alpha} = \frac{x_i}{l_h} \left[\left(1 - \frac{d\epsilon}{d\alpha} \right) \right] \quad (8.15)$$

However, a formulation is not available for neither region B nor C. In these regions, a graphical approach can be made to get the approximate slope values. Hence, “a” and “b” curves in Figure 8.5 is used to determine the downwash slopes of B and C respectively;

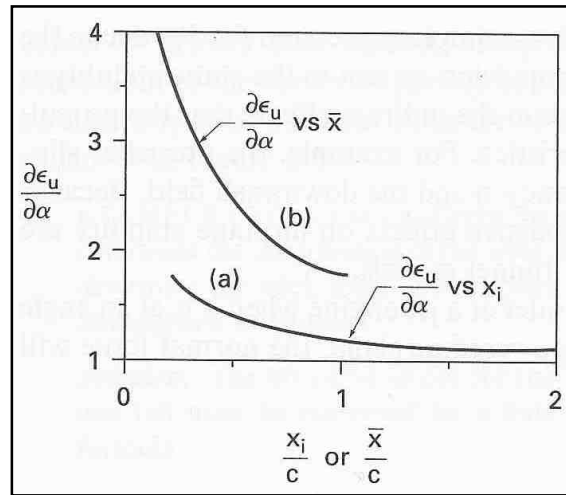


Figure 8.5 : Fuselage moment slope determination diagram

8.4 Determination of Stick Fixed Neutral Point

Neutral point or aerodynamic center of an airplane is the location, where the pitching moment does not affected by the change of angle of attack. In other words, the moment coefficient curve slope is zero. After determining the moment contributions of wing, tail and fuselage, the total pitching moment for the airplane can be written as below;

$$C_{m_\alpha} = C_{L_{\alpha_w}} \cdot \left[\frac{X_{cg}}{\bar{c}} - \frac{X_{ac}}{\bar{c}} \right] - \eta \cdot V_H C_{L_{\alpha_t}} \cdot \left(1 - \frac{d\varepsilon}{d\alpha} \right) + C_{m_{\alpha_f}} \quad (8.16)$$

As seen in Equation 8.16, moment coefficient curve slope depends on both aerodynamic characteristics and the location of center of gravity of the airplane. To find the neutral point, C_{m_α} is set as zero and the equation is being solved for the center of gravity positions. Formulation of neutral point is seen in Equation 8.17;

$$\frac{X_{np}}{\bar{c}} = \frac{X_{ac}}{\bar{c}} - \frac{C_{m_{\alpha_f}}}{C_{L_{\alpha_w}}} + \eta \cdot V_H \frac{C_{L_{\alpha_t}}}{C_{L_{\alpha_w}}} \left(1 - \frac{d\varepsilon}{d\alpha} \right) \quad (8.17)$$

After getting the neutral point formula, it can be seen that the stability is highly depends on the location of the center of gravity. In Figure 8.6, effects of the center of gravity on the airplane's stability is illustrated;

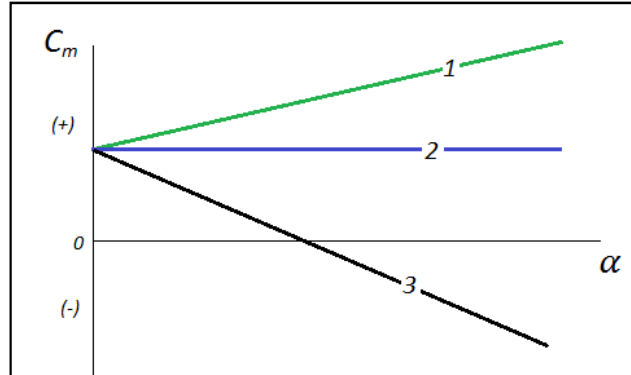


Figure 8.6 : Effects of center of gravity position on neutral point

In Figure 8.6, the green line means unstable airplane when the center of gravity placed behind the neutral point. In blue line, aircraft has neutral stability when the center of gravity placed on the neutral point. The black line represents behavior of statically stable airplane, where center of gravity placed ahead of the neutral point.

In ITU Tailsitter airplane, trim analysis has been conducted. First, the static margin is set to 5%. Second, the desired cruise speed is calculated. In the analysis, it is aimed to fly at a lift coefficient value of 0.4. As seen in Figure 8.7, the elevator angles change between -5 to +5 with 2.5 degrees of increments.

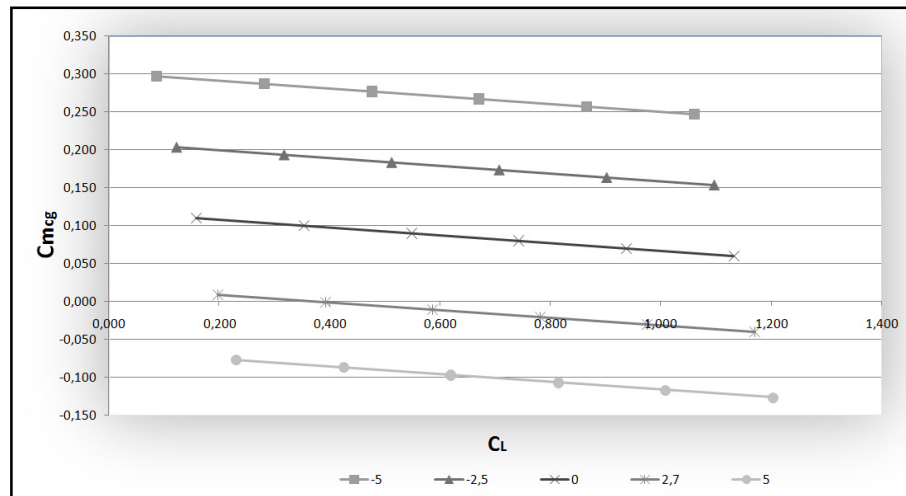


Figure 8.7 : Effects of center of gravity position on neutral point

In Figure 8.7, the vertical axis represents the change of moment coefficient, the horizontal axis represents the lift coefficient. It can be seen that, at positive 2.7 degrees of elevator angle, the airplane can be trimmed while maintaining the cruise lift coefficient; 0.4. It is also indicated that the ITU Tailsitter has negative moment slope meaning positively stable.

9. PROTOTYPING

Because of their high strength to weight ratio and good fatigue characteristics, composite materials are widely being used in aerospace industry. In ITU tailsitter airplane, carbon-kevlar hybrid fiber cloth is used. The density of the cloth used is 68 gr/m^2 . Moreover, to ensure the structural integrity and having high strength to weight ratio composite shell, sandwich shell system is used. To give a thickness to the composite shell, aramid honeycomb material having 1.5mm of thickness and 44 gr/m^2 of surface density, is used between the upper and lower layers of the composite shell. As mentioned in design section and during design calculations, aircraft weight modeling is constructed on the prototyping method. In practice, there are numerous composite production methods; pultrusion, resin transfer molding, vacuum assisted resin transfer molding, filament winding and hand lay-up. These methods have wide variety of applications from toys to full scale civil aviation or military airplanes. Pultrusion is consistent molding process. In this method, fibres are being combined with thermosetting resin; which cures under proper temperature. With the help of this method, profile or plate shaped composite materials can be easily made. The principle of pultrusion method is illustrated in Figure 9.1 below;

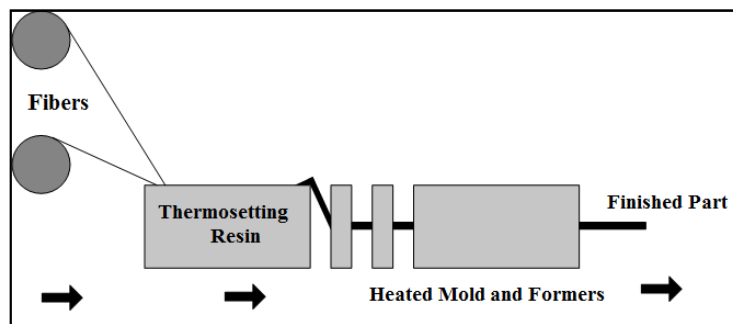


Figure 9.1 : Illustration of pultrusion method

As another method; resin transfer molding (RTM) is a type of close mold process. This is because the reinforcement material (fibers) is placed between two matching mold surfaces; one is male and the other is female. After placing the material, the mold couple is closed and thermosetting resin is injected via the injection port into

the mold. The injection process continues until the resin comes up from the vent port. The RTM method is illustrated in Figure 9.2.

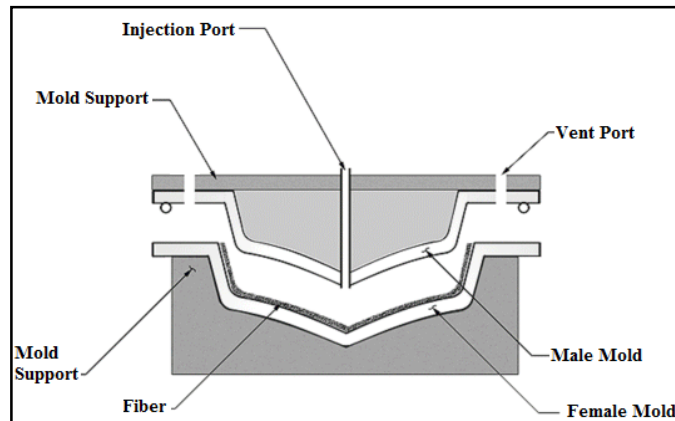


Figure 9.2 : Illustration of RTM method

In vacuum assisted resin transfer method (VARTM) is widely used in today's modern and complex structures like turbine blades, boats, cars and many other vehicles and constructions. In VARTM method, in general, female mold is used with vacuuming equipment, which works as male mold as in RTM method. This method is very useful for complex shapes and thick composite parts.

Filament winding method is generally used in the fabrication of cylindrical composite parts; like circular or rectangular cross sectional beams, composite tanks and pipes. In this method, fiber roving is wet with the resin and then wrapped onto a rotating mandrel with the specified angles. After completing the wrapping process, the resin is cured and the part is removed from the mandrel.

Composite hand lay-up method, which is decided to be used in ITU Tailsitter aircraft, is a relatively cheap production technique. For additional accuracy and strength, vacuum technique is combined with the lay-up method.

According to the fabrication method, production process has been created as below:

- A- Draw a 3D CAD model
- B- Prepare drawing for CNC machine
- C- CNC machining
- D- Apply mold releasing agent on to the mold and let it dry for 20 minutes
- E- Place carbon-kevlar fiber sheet onto the mold

- F- Wet the fiber with epoxy resin
- G- Put plastic film and blanked onto the wet fiber
- H- Cover the mold and apply vacuum

In step A, 3D cad modeling of the aircraft is obtained by using CATIA software. Because, CATIA is a valuable 3D modeling and mechanical analyze and simulation software, which is preferred by many product area from kitchen accessories to aerospace. After modeling the designed aircraft in computer environment, which is seen in Figure 9.3, the drawing is set up for the CNC machine in step B.



Figure 9.3 : 3D CAD illustration of ITU Tailsitter aircraft

Because, CNC machine accepts a generalized form of data, called G code. Step C is CNC machining stage.



Figure 9.4 : Stabilizer mold milling is in progress

In this stage, CNC machine reads the codes and mills the material, which is placed into the working area. Machining process is seen in Figure 9.4;



Figure 9.5 : Machined wing and fuselage molds

After getting the molds being machined by using CNC machine, it is time to apply wet lay-up method. In this method, epoxy or polyester resins are impregnated by hand into fibers, which are in the woven form. Rollers or brushes usually accomplish this. After that, wetted laminates are left to cure under high temperature and low-pressure condition. To give detail, some liquid mold releasing agent is applied on the mold with the help of sponge in step A. Brush or roller shouldn't be used for wetting, because surface structure of that materials are not suitable for such application.

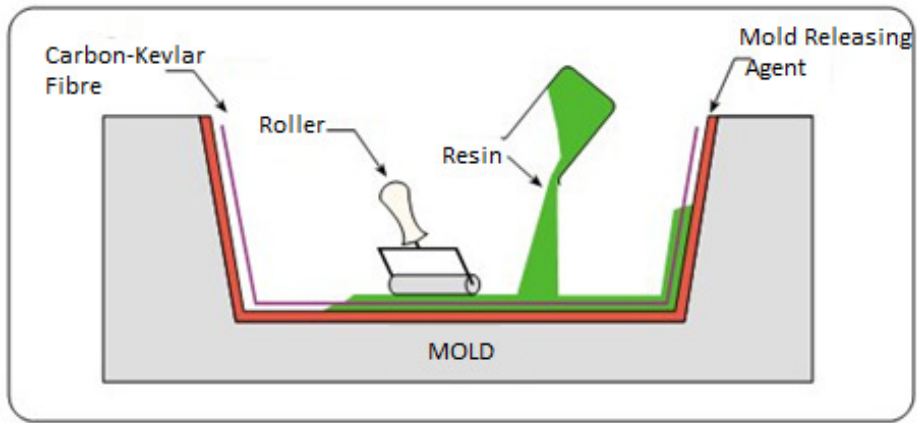


Figure 9.6 : Illustration of wet lay-up method

After 20 minutes of drying time, in step C, carbon-kevlar fibers are placed onto the mold and wet with epoxy resin by rollers or brushes. Note that, the curing time of the epoxy resin used in the production is about 24 hours.

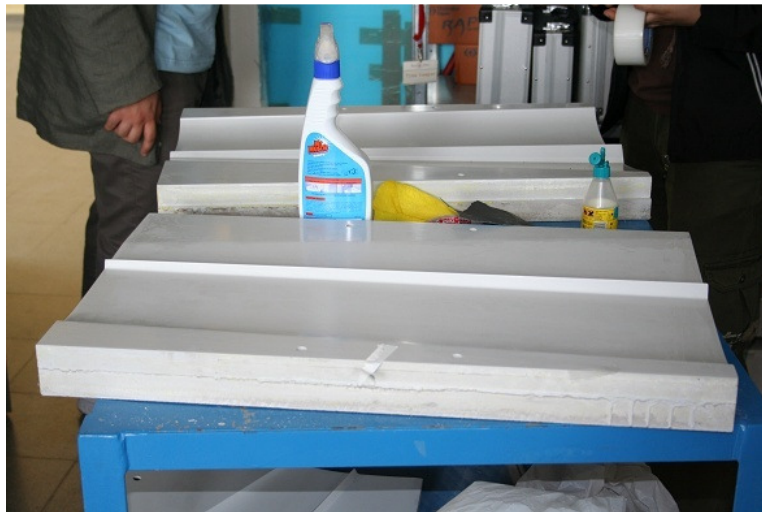


Figure 9.7 : Molds to be polished

However, the resin gets thicker after 10 minutes from stirring the compounds. In step D, plastic film having holes is applied onto the wet fibers to take out excess epoxy from the bottom layer.



Figure 9.8 : Cutting fibers for lay-up method

Meanwhile, some blankets are laid out onto the plastic film to widen the pressure created by the vacuum pump. After that, in step E, mold structure is placed into the plastic cover and vacuum is applied. A basic wet lay-up method is illustrated in Figure 9.6. Finished and polished wing molds is seen in Figure 9.7.



Figure 9.9 : Wing mold and composite wing shell

Preparation for composite lay-up method is seen in Figure 9.8. More, the mold and products are seen in Figure 9.9, 9.10 and 9.11. After the final assembly, the ITU Tailsitter airplane can be seen in Figure 9.12;



Figure 9.10 : Wing structure and molds



Figure 9.11 : Fuselage structure and mold



Figure 9.12 : ITU Tailsitter UAV

10. FLIGHT TESTS

During the design process, empirical methods are widely used to determine the aerodynamic characteristics of the airplane. So as to validate the design and see if it meets our requirements, some flight tests are conducted. Instead of using the autopilot system, manual control system with gyro assists is preferred in the first flight test. Therefore, by sensing the pitch, roll and yaw rates, the gyros help giving corrections during hover flight. The gyros to be used in the flight test were the gyros, which are commonly used in radio controlled hobby helicopters to hold their headings constant. Moreover, the radio system, which is used to control all of the control surfaces, as well as the motor controller, is Futaba brand, 10CAP model commercial hobby radio system, operating 2.4 GHz frequency. Electronic speed control unit is used to drive the brushless motor to help rotating the propeller located at the front of the airplane.

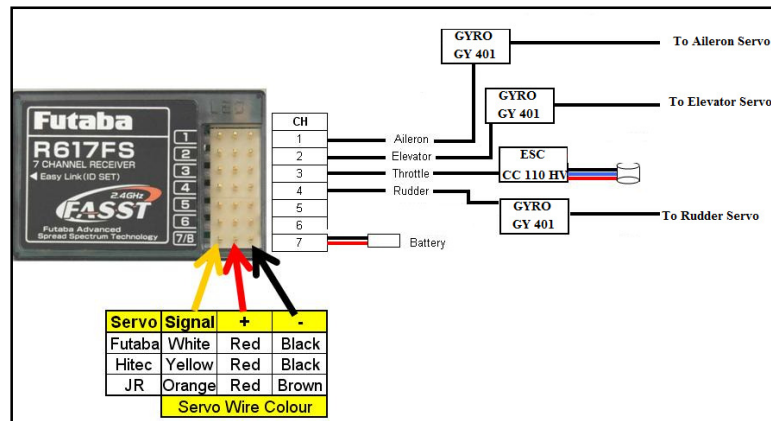


Figure 10.1 : Receiver and gyro wiring diagram

Servo motor take signals and power from the receiver and actuates the control surfaces. Therefore, to control the ailerons, elevators and rudder, five high torque servo motors are used. Wiring diagram of the components is seen in Figure 10.1. After making the electrical conncections and ensuring the structural stifness of the airframe, the aircraft is taken to the flight field to see the hoverin performance.

Hovering is one of the flight phases in which the aircraft holds its vertical position and hangs on its propeller as seen in Figure 10.2



Figure 10.2 : ITU Tailsitter is ready for the flight test

After setting up the airplane, the flight sequence is started by holding the wing tips by two people, as seen in Figure 10.3.



Figure 10.3 : Beginning of the flight test

However, as seen in Figure 10.4, the person located at the left side of the airplane, was late to release the airplane.



Figure 10.4 : ITU Tailsitter is ready for the flight test

As a result, instead of climbing vertically, the aircraft couldn't maintain its position and started low speed high angle of attack flight, which is not suitable for its nature.



Figure 10.5 : ITU Tailsitter is taking off

Therefore, after 10 seconds from taking off, the aircraft crashed because of the controllability problems due to the disturbance given in the take off phase. In addition to the disturbance during take-off, lack of authority on the control surfaces is affected by the flying weight of the aircraft. Because, the flying weight of the aircraft is determined as 10kg. However, it was only 7 kg during the flight tests.

Weight of the airplane affects the propeller's RPM. Therefore, the lower RPM means lower airspeed behind the propeller. In hover mode, the forces generated by the control surfaces is highly related to the airspeed coming from the propeller. As a result, the lower speed coming from the propeller makes the control surfaces generate lower forces to control the aircraft's behavior.

11. CONCLUSION AND RECOMMENDATIONS

In this work, the design optimization study of a tailsitter aircraft with a revolutionary hybrid/dual propulsion system has been described. The obtained results in this thesis are based on analytical calculations on the propeller propulsion system, experimental data on the EDF propulsion system and the design inputs which are in close relation with both the design constraints and design criteria.

Initial system performance analysis with candidate propulsion units indicate that up to 27.5 m/s cruise speed and maximum 2 hours of flight endurance, including 3 minutes of vertical take-off and landing duration, can be achieved while carrying a 1 kg payload and 90 km of range – a marvelous performance in comparison to the same class rotary-wing and OAV alternatives.

Prototyping of ITU Tailsitter is completed and flight tests were conducted. According to the flight tests, even if the airplane crashed, controllability of the airplane under hover or low speed flight regimes, has been proven.

In order to see and validate the cruise performance, more flight tests can be made.

REFERENCES

- [1] **R. Beard, D. Kingston, M. Quigley, D. Snyder, R. Christiansen, W. Johnson, T. McLain, and M. Goodrich**, *Autonomous vehicle technologies for small fixed wing UAVs*, AIAA Journal of Aerospace, Computing, Information, and Communication, 2(1):92–108, 2005.
- [2] **N.B. Knoebel**, *Adaptive Quaternion Control of a Miniature Tailsitter UAV*, PhD thesis, Brigham Young University, 2007.
- [3] **S. Ates, I. Bayezit and G. Inalhan**, *Design and HIL Integration of a UAV Microavionics System in a Manned—Unmanned Joint Airspace Flight Network Simulator*, Journal of Intelligent and Robotic Systems, 54(1-3):359–386, 2009.
- [4] **R.H. Stone**, *The T-wing tail-sitter research UAV*, In International Powered Lift Conference, Williamsburg, Virginia, 2002.
- [5] **N.B.K.S.R. Osborne, D.O. Snyder, T.W.M.L.R.W. Beard, and A.M. Eldredge**, *Preliminary modeling, control, and trajectory design for miniature autonomous tailsitters*, AIAA Guidance, Navigation, and Control Conference and Exhibit, 2006.
- [6] **S. Shkarayev, J.M. Moschetta, and B. Bataille**, *Aerodynamic design of micro air vehicles for vertical flight*, Journal of Aircraft , 45(5):1715–1724, 2008.
- [7] **Torres G. E. Mueller, T. J. and D. W. Srull**, *Introduction to the Design of Fixed-Wing Micro Aerial Vehicles* , chapter 5, page 391. AIAA, 2006[3]
- [8] **Url-1** <http://home.vrweb.de/schuebeler.impeller/messungen_e.html>, retrieved 10 January 2008
- [9] **Merchant, M. P.**, *Propeller Performance Measurement for Low Reynolds Number Unmanned Aerial Vehicle Applications*, Wichita State University, Kansas, Wichita, 2005
- [10] **Url-2** <<http://www.mh-aerotools.de/airfoils/javaprop.htm>>, retrieved on March 2009
- [11] **Url-3** <<http://www.drivecalc.de/PropCalc/index.html>>, retrieved on January 2009
- [12] **Url-4** <http://www.icare-rc.com/plettenberg_predator.htm>, retrieved on January 2008
- [13] **Darrol Stinton**, *The Design of The Aeroplane*, chapter: Reciprocating Engines, pages 308–310. BSP Professional Books, 1993.

- [14] **R.H. Stone**, *The T-wing tail-sitter research UAV*, In International Powered Lift Conference, Williamsburg, Virginia, 2002.
- [15] **Daniel P. Raymer**, *Aircraft Design: A Conceptual Approach*, chapter Aerodynamics, pages 280–288. American Institute of Aeronautics and Astronautics, 2nd edition, 1992.
- [16] **Url-5** <<http://www.esteco.com/>>
- [17] **ModeFRONTIER 3.2**, Help Menu
- [18] **Arora, Jasbir S.**, *Introduction To Optimum Design*, Elsevier Academic Press, 2004, Second Edition, London
- [19] **Singiresu S. Rao**, *Engineering Optimization*, Printed in the United States of America, 1996 by John Wiley & Sons, Inc., Wiley Eastern Limited, Publishers, and New Age International Publishers, Ltd.
- [20] **Tomas Melin**, *A Vortex Lattice MATLAB Implementation for Linear aerodynamic Wing Applications*, Master Thesis, Royal Institute of Technology (KTH), December 2000.
- [21] **Multhopp, H.**, , *Aerodynamics of Fuselage*, NACA-TM 1036, 1942

CURRICULUM VITA



Candidate's full name: Miraç Kuddusi Aksugür

Place and date of birth: Tekirdağ, 1983

Permanent Address: Yeşilce mah., Seçilmiş Sokak, No:42/2, Kağıthane, İstanbul

Universities and

Colleges attended: Istanbul Technical University, Aerospace Engineering (2000-2007)

Publications:

- **Aksugur, M.**, Inalhan, G., *Design Methodology of a Hybrid Propulsion Driven Electric Powered Miniature Tailsitter Unmanned Aerial Vehicle*, Springer Netherlands, Journal of Intelligent and Robotic Systems, Vol 57, p: 359-386 March 2010
- **Aksugur, M.**, Inalhan, G., Beard, R., *Hybrid Propulsion System Design of a VTOL Tailsitter UAV*, Unmanned Aerial Vehicles 2008, SAE, 2008, ISBN-10: 0768020565, ISBN-13: 978- 0768020564
- Ates, S., Beyazit, I., **Aksugur, M.**, Inalhan, G., The Autonomy of Fixed-Wing Aerial Vehicles and Experimental Design Steps on Implementing Autonomous Navigation, Landing and Take-Off Operations for the Trainer 60 Model Aircraft, 5. Ankara International aerospace Conference, Ankara Türkiye 17-19 Ağustos 2009
- **Aksugur, M.**, Inalhan, G., *Design Methodology of a Hybrid Propulsion Driven Electric Powered Miniature Tailsitter Unmanned Aerial Vehicle*, Second

Symposium on Unmanned Aerial Vehicles, Reno, Nevada, ABD, 8-10 Haziran, 2009

- **Aksugur, M.**, Inalhan, G., Beard, R., *Hybrid Propulsion System Design of a VTOL Tailsitter UAV*, Wichita Aviation Technology Congress, Wichita, Kansas, ABD, 19-21 Ağustos, 2008
- Ates, S., Beyazit, I., Gunduz, F.E., **Aksugur, M.**, Armagan, B., Inalhan, G., *Design and Hardware-in-the-Loop Integration of a UAV Micro Avionics System in a Manned-Unmanned Joint Airspace Flight Network Simulator*, UAV'08 Conference, Orlando Florida, ABD 23-25 Haziran 2008
- **Aksugur, M.**, et. al., *A Design Approach and Optimization Techniques for the Aircraft Design Contest with a Constrained Propulsion System, Wing Span and Take-Off Distance*, Ankara International Aerospace Conference, Ankara, Türkiye, 27-29 Eylül, 2007.
- Karaman, S., **Aksugur, M.**, Baltacı, T., Bronz, M., Kurtulus, C., Inalhan, G., Altug, E., Guvenc, L., *Aricopter: Aerobotic Platform for Advances in Flight, Vision Controls and Distributed Autonomy*, IEEE Intelligent Vehicles Symposium, Istanbul, Türkiye, 13-15 Haziran, 2007.
- Cetinkaya, A., Karaman, S., Arslan, O., **Aksugur M.**, G. Inalhan, *Design of a Distributed C2 Architecture for Interoperable Manned/Unmanned Fleets*, 7th International Conference on Cooperative Control and Optimization, Florida, ABD, 31 Ocak- 2 Subat, 2007
- **Aksugur, M.**, Karagoz, M., *Öğrenci Yarışma Projelerinin Mühendislik Gelişimine Katkıları*, TMMOB 4. Havacılık ve Uzay Mühendisliği Çalıştayı, Eskişehir, Türkiye, Mart 2007

**DIKEY İNİŞ KALKIŞ YAPABİLEN HİBRİT İTKİ SİSTEMLİ BİR
İNSANSIZ HAVA ARACININ ÖN TASARIMI, ÜRETİMİ VE TEST UÇUŞU
ÇALIŞMALARI**

**YÜKSEK LİSANS TEZİ
Miraç K. AKSUGÜR
(511071149)**

**Tezin Enstitüye Verildiği Tarih : 24 Kasım 2010
Tezin Savunulduğu Tarih : 12 Kasım 2010**

**Tez Danışmanı : Doç. Dr. Gökhan İNALHAN (İTÜ)
Diğer Jüri Üyeleri : Prof. Dr. Mehmet Ş. KAVSAOĞLU (İTÜ)
Doç. Dr. M. Turan SÖYLEMEZ (İTÜ)
Tez Danışmanı : Doç. Dr. Gökhan İNALHAN (İTÜ)**

KASIM 2010